

A search for leptoquark bosons and lepton flavor violation in e^+p collisions at HERA

The H1 Collaboration

C. Adloff³³, V. Andreev²⁴, B. Andrieu²⁷, V. Arkadov³⁴, A. Astvatsatourov³⁴, I. Ayyaz²⁸, A. Babaev²³, J. Bähr³⁴, P. Baranov²⁴, E. Barrelet²⁸, W. Bartel¹⁰, U. Bassler²⁸, P. Bate²¹, A. Beglarian^{10,39}, O. Behnke¹⁰, H.-J. Behrend¹⁰, C. Beier¹⁴, A. Belousov²⁴, Ch. Berger¹, G. Bernardi²⁸, T. Berndt¹⁴, G. Bertrand-Coremans⁴, P. Biddulph²¹, J.C. Bizot²⁶, V. Boudry²⁷, W. Braunschweig¹, V. Brisson²⁶, H.-B. Bröker², D.P. Brown²¹, W. Brückner¹², P. Bruel²⁷, D. Bruncko¹⁶, J. Bürger¹⁰, F.W. Büsler¹¹, A. Bunyatyan^{12,39}, S. Burke¹⁷, A. Burrage¹⁸, G. Buschhorn²⁵, D. Calvet²², A.J. Campbell¹⁰, T. Carli²⁵, E. Chabert²², M. Charlet⁴, D. Clarke⁵, B. Clerbaux⁴, J.G. Contreras^{7,42}, C. Cormack¹⁸, J.A. Coughlan⁵, M.-C. Cousinou²², B.E. Cox²¹, G. Cozzika⁹, J. Cvach²⁹, J.B. Dainton¹⁸, W.D. Dau¹⁵, K. Daum³⁸, M. David^{9,i}, M. Davidsson²⁰, A. De Roeck¹⁰, E.A. De Wolf⁴, B. Delcourt²⁶, R. Demirchyan^{10,40}, C. Diaconu²², M. Dirkmann⁷, P. Dixon¹⁹, V. Dodonov¹², K.T. Donovan¹⁹, J.D. Dowell³, A. Droustskoi²³, J. Ebert³³, G. Eckerlin¹⁰, D. Eckstein³⁴, V. Efremenko²³, S. Egli³⁶, R. Eichler³⁵, F. Eisele¹³, E. Eisenhandler¹⁹, E. Elsen¹⁰, M. Enzenberger²⁵, M. Erdmann^{13,41,f}, A.B. Fahr¹¹, P.J.W. Faulkner³, L. Favart⁴, A. Fedotov²³, R. Felst¹⁰, J. Feltesse⁹, J. Ferencei¹⁰, F. Ferrarotto³¹, S. Ferron²⁷, M. Fleischer¹⁰, G. Flügge², A. Fomenko²⁴, J. Formánek³⁰, J.M. Foster²¹, G. Franke¹⁰, E. Gabathuler¹⁸, K. Gabathuler³², F. Gaede²⁵, J. Garvey³, J. Gassner³², J. Gayler¹⁰, R. Gerhards¹⁰, S. Ghazaryan^{10,39}, A. Glazov³⁴, L. Goerlich⁶, N. Gogitidze²⁴, M. Goldberg²⁸, I. Gorelov²³, C. Grab³⁵, H. Grässler², T. Greenshaw¹⁸, R.K. Griffiths¹⁹, G. Grindhammer²⁵, T. Hadig¹, D. Haidt¹⁰, L. Hajduk⁶, M. Hampel¹, V. Haustein³³, W.J. Haynes⁵, B. Heinemann¹⁰, G. Heinzelmann¹¹, R.C.W. Henderson¹⁷, S. Hengstmann³⁶, H. Henschel³⁴, R. Heremans⁴, G. Herrera^{7,43,l}, I. Herynek²⁹, K. Hewitt³, M. Hilgers³⁵, K.H. Hiller³⁴, C.D. Hilton²¹, J. Hladký²⁹, P. Höting², D. Hoffmann¹⁰, R. Horisberger³², S. Hurling¹⁰, M. Ibbotson²¹, Ç. İssever⁷, M. Jacquet²⁶, M. Jaffre²⁶, L. Janauschek²⁵, D.M. Jansen¹², L. Jönsson²⁰, D.P. Johnson⁴, M. Jones¹⁸, H. Jung²⁰, H.K. Kästli³⁵, M. Kander¹⁰, D. Kant¹⁹, M. Kapichine⁸, M. Karlsson²⁰, O. Karschnick¹¹, O. Kaufmann¹³, M. Kausch¹⁰, F. Keil¹⁴, N. Keller¹³, I.R. Kenyon³, S. Kermiche²², C. Kiesling²⁵, M. Klein³⁴, C. Kleinwort¹⁰, G. Knies¹⁰, J.H. Köhne²⁵, H. Kolanoski³⁷, S.D. Kolya²¹, V. Korbel¹⁰, P. Kostka³⁴, S.K. Kotelnikov²⁴, T. Krämerkämper⁷, M.W. Krasny²⁸, H. Krehbiel¹⁰, D. Krücker²⁵, K. Krüger¹⁰, A. Küpper³³, H. Küster², M. Kuhlen²⁵, T. Kurča³⁴, W. Lachnit¹⁰, R. Lahmann¹⁰, D. Lamb³, M.P.J. Landon¹⁹, W. Lange³⁴, U. Langenegger³⁵, A. Lebedev²⁴, F. Lehner¹⁰, V. Lemaître¹⁰, R. Lemrani¹⁰, V. Lendermann⁷, S. Levonian¹⁰, M. Lindstroem²⁰, G. Lobo²⁶, E. Lobodzinska^{6,40}, V. Lubimov²³, S. Lüders³⁵, D. Lüke^{7,10}, L. Lytkin¹², N. Magnussen³³, H. Mahlke-Krüger¹⁰, N. Malden²¹, E. Malinovski²⁴, I. Malinovski²⁴, R. Maraček²⁵, P. Marage⁴, J. Marks¹³, R. Marshall²¹, H.-U. Martyn¹, J. Martyniak⁶, S.J. Maxfield¹⁸, T.R. McMahon¹⁸, A. Mehta⁵, K. Meier¹⁴, P. Merkel¹⁰, F. Metlica¹², A. Meyer¹⁰, H. Meyer³³, J. Meyer¹⁰, P.-O. Meyer², S. Mikocki⁶, D. Milstead¹⁸, R. Mohr²⁵, S. Mohrdieck¹¹, M.N. Mondragon⁷, F. Moreau²⁷, A. Morozov⁸, J.V. Morris⁵, D. Müller³⁶, K. Müller¹³, P. Murín^{16,44}, V. Nagovizin²³, B. Naroska¹¹, J. Naumann⁷, Th. Naumann³⁴, I. Négre²², P.R. Newman³, H.K. Nguyen²⁸, T.C. Nicholls¹⁰, F. Niebergall¹¹, C. Niebuhr¹⁰, Ch. Niedzballa¹, H. Niggli³⁵, O. Nix¹⁴, G. Nowak⁶, T. Nunnemann¹², H. Oberlack²⁵, J.E. Olsson¹⁰, D. Ozerov²³, P. Palmen², V. Panassik⁸, C. Pascaud²⁶, S. Passaggio³⁵, G.D. Patel¹⁸, H. Pawletta², E. Perez⁹, J.P. Phillips¹⁸, A. Pieuchot¹⁰, D. Pitzl³⁵, R. Pöschl⁷, I. Potashnikova¹², B. Povh¹², K. Rabbertz¹, G. Rädcl⁹, J. Rauschenberger¹¹, P. Reimer²⁹, B. Reisert²⁵, D. Reyna¹⁰, S. Riess¹¹, E. Rizvi³, P. Robmann³⁶, R. Roosen⁴, K. Rosenbauer¹, A. Rostovtsev^{23,10}, C. Royon⁹, S. Rusakov²⁴, K. Rybicki⁶, D.P.C. Sankey⁵, P. Schacht²⁵, J. Scheins¹, F.-P. Schilling¹³, S. Schleich¹⁴, P. Schleper¹³, D. Schmidt³³, D. Schmidt¹⁰, L. Schoeffel⁹, T. Schörner²⁵, V. Schröder¹⁰, H.-C. Schultz-Coulon¹⁰, F. Sefkow³⁶, V. Shekelyan²⁵, I. Sheviakov²⁴, L.N. Shtarkov²⁴, G. Siegmund¹⁵, Y. Sirois²⁷, T. Sloan¹⁷, P. Smirnov²⁴, M. Smith¹⁸, V. Solochenko²³, Y. Soloviev²⁴, V. Spakov⁸, A. Specka²⁷, H. Spitzer¹¹, F. Squinabol²⁶, R. Stamen⁷, J. Steinhart¹¹, B. Stella³¹, A. Stellberger¹⁴, J. Stiewe¹⁴, U. Straumann¹³, W. Struczynski², J.P. Sutton³, M. Swart¹⁴, S. Tapprogge¹⁴, M. Tasevsky²⁹, V. Tchernyshov²³, S. Tchetchelnitski²³, G. Thompson¹⁹, P.D. Thompson³, N. Tobien¹⁰, R. Todenhausen¹², D. Traynor¹⁹, P. Truöl³⁶, G. Tsipolitis³⁵, J. Turnau⁶, E. Tzamariudaki²⁵, S. Udluft²⁵, A. Usik²⁴, S. Valkár³⁰, A. Valkárová³⁰, C. Vallée²², A. Van Haecke⁹, P. Van Mechelen⁴, Y. Vazdik²⁴, G. Villet⁹, K. Wacker⁷, R. Wallny¹³, T. Walter³⁶, B. Waugh²¹, G. Weber¹¹, M. Weber¹⁴, D. Wegener⁷, A. Wegner¹¹, T. Wengler¹³, M. Werner¹³, L.R. West³, G. White¹⁷, S. Wiesand³³, T. Wilksen¹⁰, M. Winde³⁴, G.-G. Winter¹⁰, Ch. Wissing⁷, C. Wittek¹¹, M. Wobisch², H. Wollatz¹⁰, E. Wünsch¹⁰, J. Žáček³⁰, J. Zálešák³⁰, Z. Zhang²⁶, A. Zhokin²³, P. Zimi²⁸, F. Zomer²⁶, J. Zsembery⁹, and M. zur Nedden¹⁰

- ¹ I. Physikalisches Institut der RWTH, Aachen, Germany^a
- ² III. Physikalisches Institut der RWTH, Aachen, Germany^a
- ³ School of Physics and Space Research, University of Birmingham, Birmingham, UK^b
- ⁴ Inter-University Institute for High Energies ULB-VUB, Brussels; Universitaire Instelling Antwerpen, Wilrijk; Belgium^c
- ⁵ Rutherford Appleton Laboratory, Chilton, Didcot, UK^b
- ⁶ Institute for Nuclear Physics, Cracow, Poland^d
- ⁷ Institut für Physik, Universität Dortmund, Dortmund, Germany^a
- ⁸ Joint Institute for Nuclear Research, Dubna, Russia
- ⁹ DSM/DAPNIA, CEA/Saclay, Gif-sur-Yvette, France
- ¹⁰ DESY, Hamburg, Germany^a
- ¹¹ II. Institut für Experimentalphysik, Universität Hamburg, Hamburg, Germany^a
- ¹² Max-Planck-Institut für Kernphysik, Heidelberg, Germany^a
- ¹³ Physikalisches Institut, Universität Heidelberg, Heidelberg, Germany^a
- ¹⁴ Institut für Hochenergiephysik, Universität Heidelberg, Heidelberg, Germany^a
- ¹⁵ Institut für experimentelle und angewandte Physik, Universität Kiel, Kiel, Germany^a
- ¹⁶ Institute of Experimental Physics, Slovak Academy of Sciences, Košice, Slovak Republic^{e,i}
- ¹⁷ School of Physics and Chemistry, University of Lancaster, Lancaster, UK^b
- ¹⁸ Department of Physics, University of Liverpool, Liverpool, UK^b
- ¹⁹ Queen Mary and Westfield College, London, UK^b
- ²⁰ Physics Department, University of Lund, Lund, Sweden^f
- ²¹ Department of Physics and Astronomy, University of Manchester, Manchester, UK^b
- ²² CPPM, Université d'Aix-Marseille II, IN2P3-CNRS, Marseille, France
- ²³ Institute for Theoretical and Experimental Physics, Moscow, Russia
- ²⁴ Lebedev Physical Institute, Moscow, Russia^{e,j}
- ²⁵ Max-Planck-Institut für Physik, München, Germany^a
- ²⁶ LAL, Université de Paris-Sud, IN2P3-CNRS, Orsay, France
- ²⁷ LPNHE, École Polytechnique, IN2P3-CNRS, Palaiseau, France
- ²⁸ LPNHE, Universités Paris VI and VII, IN2P3-CNRS, Paris, France
- ²⁹ Institute of Physics, Academy of Sciences of the Czech Republic, Praha, Czech Republic^{e,g}
- ³⁰ Nuclear Center, Charles University, Praha, Czech Republic^{e,g}
- ³¹ INFN Roma 1 and Dipartimento di Fisica, Università Roma 3, Roma, Italy
- ³² Paul Scherrer Institut, Villigen, Switzerland
- ³³ Fachbereich Physik, Bergische Universität Gesamthochschule Wuppertal, Wuppertal, Germany^a
- ³⁴ DESY, Zeuthen, Germany^a
- ³⁵ Institut für Teilchenphysik, ETH, Zürich, Switzerland^h
- ³⁶ Physik-Institut der Universität Zürich, Zürich, Switzerland^h
- ³⁷ Institut für Physik, Humboldt-Universität, Berlin, Germany^a
- ³⁸ Rechenzentrum, Bergische Universität Gesamthochschule Wuppertal, Wuppertal, Germany^a
- ³⁹ Visitor from Yerevan Physics Institute, Armenia
- ⁴⁰ Foundation for Polish Science fellow
- ⁴¹ Institut für Experimentelle Kernphysik, Universität Karlsruhe, Karlsruhe, Germany
- ⁴² Department Fis. Ap. CINVESTAV, Mérida, Yucatán, México
- ⁴³ On leave from CINVESTAV, México
- ⁴⁴ University of P.J. Šafárik, SK-04154 Košice, Slovak Republic

Received: 2 July 1999 / Published online: 28 September 1999

Dedicated to the memory of our colleague and friend Marc David, deceased 23.01.99.

Abstract. A search for new bosons possessing couplings to lepton-quark pairs is performed in the H1 experiment at HERA using 1994 to 1997 data corresponding to an integrated luminosity of 37 pb^{-1} . First generation leptoquarks (LQs) are searched in very high Q^2 neutral (NC) and charged (CC) current data samples. The measurements are compared to Standard Model (SM) expectations from deep-inelastic scattering (DIS). A deviation in the Q^2 spectrum previously observed in the 1994 to 1996 dataset at $Q^2 \gtrsim 15000 \text{ GeV}^2$ remains, though with less significance. This deviation corresponded to a clustering in the invariant mass spectrum at $M \simeq 200 \text{ GeV}$ which is not observed with the 1997 dataset alone. The NC DIS data is used to constrain the Yukawa couplings λ of first generation scalar and vector LQs in the Buchmüller–Rückl–Wyler effective model. Scalar LQs are excluded for masses up to 275 GeV for a coupling of electromagnetic strength, $\lambda = 0.3$. A sensitivity to coupling values $\lesssim 1$ is established for masses up to 400 GeV for any LQ type. The NC and CC DIS data are combined to constrain λ for arbitrary branching ratios of the LQ into

eq in a generic model. For a decay branching ratio into e^+u pairs as small as 10%, LQ masses up to 260 GeV are ruled out for $\lambda = 0.3$. LQs possessing couplings to mixed fermion generations, which could lead to signals of lepton flavor violation (LFV), are searched in events with a high transverse momentum μ or τ . No $\mu + X$ or $\tau + X$ event candidate is found that is compatible with LQ kinematics. Constraints are set on the Yukawa coupling involving the μ and τ lepton in a yet unexplored mass range.

1 Introduction

The ep collider HERA offers the unique possibility to search for s -channel production of new particles which couple to lepton-parton pairs. Examples are leptoquark (LQ) colour triplet bosons which appear naturally in various unifying theories beyond the Standard Model (SM) such as Grand Unified Theories [1] and Superstring inspired E_6 models [2], and in some Compositeness [3] and Technicolour [4] models. Leptoquarks could be singly produced by the fusion of the 27.5 GeV initial state lepton with a quark of the 820 GeV incoming proton, with masses up to the kinematic limit of $\sqrt{s_{ep}} \simeq 300$ GeV.

The interest in such new bosons has been considerably renewed recently following the observation by the H1 [5] and ZEUS [6] experiments of a possible excess of events at very high masses and squared momentum transfer Q^2 , above expectations from SM neutral current (NC) and charged current (CC) deep-inelastic scattering (DIS). These early results were based on data samples collected from 1994 to 1996. Of particular interest was the apparent “clustering” of outstanding NC events at masses around 200 GeV observed in H1 which has motivated considerable work on LQ kinematics [7], constraints and phenomenology [8], extending beyond the original effective model of Buchmüller-Rückl-Wyler (BRW) [9].

In this paper, LQs are searched using all available e^+p data collected in H1 from 1994 to 1997. Inclusive single and double differential DIS cross-sections obtained from a similar dataset are presented in a separate paper [10]. Here, firstly, NC and CC measurements at high Q^2 are compared with SM expectations at detector level. Mass

and angular distributions of NC- and CC-like events are then used to set constraints on first generation LQs. The search is then further extended to LQs possessing couplings to leptons of different generations. Such lepton flavor violating (LFV) LQs would lead to final states involving a second or third generation lepton.

The total integrated luminosity \mathcal{L} amounts to 37 pb^{-1} , an increase in statistics of a factor ~ 2.6 compared to previous H1 analysis at very high Q^2 [5] and a factor ~ 13 compared to previous LQ searches at HERA [11–13].

2 The H1 detector

A complete description of the H1 detector can be found elsewhere [14]. Here we introduce only the components relevant for the present analysis in which the final state of the processes involves either a charged lepton¹ with high transverse energy or a large amount of hadronic transverse energy flow.

Positron energies and angles are measured in a liquid argon (LAr) sampling calorimeter [15] covering the polar angular² range $4^\circ \leq \theta \leq 154^\circ$ and all azimuthal angles. The LAr calorimeter is divided in eight “wheels” along the beam axis, themselves subdivided in up to 8 modules with minimum inactive material (“cracks”) in between. The modules consist of a lead/argon electromagnetic section followed by a stainless steel/argon hadronic section. Their fine read-out granularity is optimized to provide approximately uniform segmentation in laboratory pseudo-rapidity and azimuthal angle ϕ . Electromagnetic shower energies are measured with a resolution of $\sigma(E)/E \simeq 12\%/\sqrt{E/\text{GeV}} \oplus 1\%$ and pion induced hadronic energies with $\sigma(E)/E \simeq 50\%/\sqrt{E/\text{GeV}} \oplus 2\%$ after software energy weighting. These energy resolutions were measured in test beams with electron energies up to 166 GeV [16, 17] and pion energies up to 205 GeV [17]. The energy calibration was determined initially from test beam data with an uncertainty of 3% and 4% for electromagnetic and hadronic energies respectively. A new absolute energy scale calibration for positrons detected in the actual H1 experiment has been recently established [10, 18] *in situ* by using the over-constrained kinematics of NC DIS, QED Compton and e^+e^- pair production from two-photon processes. A precision of 0.7% is reached in the LAr central barrel region $80^\circ \lesssim \theta_e \lesssim 145^\circ$, 1.5% in $40^\circ \lesssim \theta_e \lesssim 80^\circ$ and

¹ The analysis does not distinguish explicitly between + and – charges

² The z axis is taken to be in the direction of the incident proton, the forward direction, and the origin of coordinates is the nominal ep interaction point

[†] Deceased

^a Supported by the Bundesministerium für Bildung, Wissenschaft, Forschung und Technologie, FRG, under contract numbers 7AC17P, 7AC47P, 7DO55P, 7HH17I, 7HH27P, 7HD17P, 7HD27P, 7KI17I, 6MP17I and 7WT87P

^b Supported by the UK Particle Physics and Astronomy Research Council, and formerly by the UK Science and Engineering Research Council

^c Supported by FNRS-FWO, IISN-IKW

^d Partially supported by the Polish State Committee for Scientific Research, grant no. 115/E-343/SPUB/P03/002/97 and grant no. 2P03B 055 13

^e Supported by the Deutsche Forschungsgemeinschaft

^f Supported by the Swedish Natural Science Research Council

^g Supported by GA ČR grant no. 202/96/0214, GA AV ČR grant no. A1010821 and GA UK grant no. 177

^h Supported by the Swiss National Science Foundation

ⁱ Supported by VEGA SR grant no. 2/5167/98

^j Supported by Russian Foundation for Basic Research grant no. 96-02-00019

3.0% in the forward region $5^\circ \lesssim \theta_e \lesssim 40^\circ$. The precision on the hadronic energy scale was determined by requiring the balance of the transverse momenta of the positron and hadronic system in NC DIS events. This was performed using a method [10] correcting the energy flow associated to jets by LAr wheel calibration constants. The hadronic energy scale is found to be understood at the 2% level when comparing to Monte Carlo expectation. This represents an improved understanding of both the electromagnetic and hadronic energy scales compared to [5], made possible by the increase of statistics accumulated in 1997. All analyses described in the following rely on this updated calibration. The resolution on the polar angle of the positron measured from the electromagnetic shower in the calorimeter varies from ~ 2 mrad below 30° to $\lesssim 5$ mrad at larger angles. A lead/scintillating-fibre backward calorimeter [19] extends the coverage³ at larger angles ($153^\circ \leq \theta \lesssim 178^\circ$).

Located inside the calorimeters is the tracking system which is used here to determine the interaction vertex and provide charged track information relevant for lepton identification (see Sect. 5). The main components of this system are central drift and proportional chambers ($25^\circ \leq \theta \leq 155^\circ$), a forward track detector ($7^\circ \leq \theta \leq 25^\circ$) and a backward drift chamber³. The tracking chambers and calorimeters are surrounded by a superconducting solenoid providing a uniform field of 1.15 T parallel to the z axis within the detector volume. The instrumented iron return yoke surrounding this solenoid is used to measure leakage of hadronic showers and to recognize muons. The luminosity is determined from the rate of the Bethe-Heitler $ep \rightarrow ep\gamma$ bremsstrahlung measured in a luminosity monitor. This consists of a positron tagger and a photon tagger located along the beam line, -33 m and -103 m respectively from the interaction point.

For the acquisition of events we rely on the timing information from a time-of-flight system and on the LAr trigger system which provides a measurement of the energy flow using coarse trigger towers [15].

3 Leptoquark phenomenology and models

Leptoquark production at HERA can lead to final states similar to those of DIS physics at very high Q^2 . The basic DIS processes are illustrated in Fig. 1a. Leptoquarks can be resonantly produced in the s -channel and exchanged in the u -channel as illustrated by the diagrams in Fig. 1b,c. Here and in the following, whenever specified, the indices i and j of the couplings λ_{ij} at the LQ–lepton–quark vertices refer to the lepton i^{th} and quark j^{th} generation respectively. Otherwise, λ designates a coupling of LQs to first generation fermions (henceforth called first generation LQs) give $e+q$ or $\nu+q'$ final states leading to individual events indistinguishable from SM NC and CC DIS respectively. LQs with LFV couplings to second or third generation

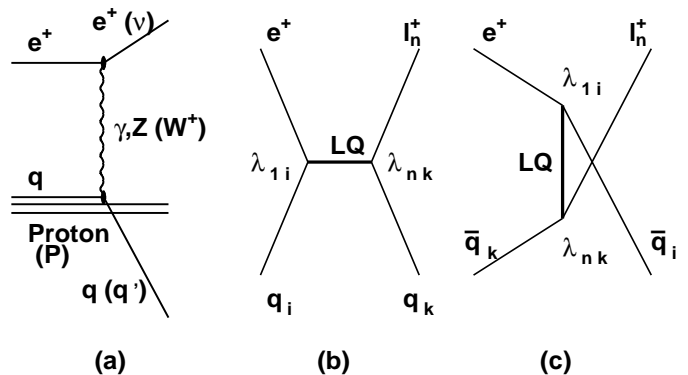


Fig. 1a–c. Diagrams of (a) deep-inelastic scattering; (b) s -channel resonant production and (c) u -channel exchange of a leptoquark with fermion number $F = 0$. Diagrams involving a $|F| = 2$ leptoquark are obtained from (b) and (c) by exchanging q and \bar{q}

leptons (henceforth called LFV LQs) can participate in $e^+p \rightarrow \mu^+ + jet + X$ or $e^+p \rightarrow \tau^+ + jet + X$ processes. Such exotic signatures are expected to be essentially background free for high transverse momentum of the observable lepton.

In the s -channel, a LQ is produced at a mass $M = \sqrt{s_{ep}x}$ where x is the momentum fraction of the proton carried by the struck quark. Over a large fraction of the mass range accessible at HERA and for a reasonable coupling strength, e.g. satisfying $\lambda^2/4\pi < 1$, the intrinsic decay width of a scalar (S) or vector (V) LQ of nominal mass M_{LQ} into a lepton and a quark is expected to be small. This width is calculated as $\Gamma_S = (3/2)\Gamma_V = \lambda_{ij}^2 M_{LQ}/16\pi$ which corresponds for example to $\Gamma_S \simeq 40$ MeV for a scalar at $M_{LQ} = 200$ GeV and $\lambda_{ij} = 0.1$. In the narrow-width approximation (NWA), the resonant production cross-section σ_{NWA} is proportional to $\lambda^2 q(x)$ where $q(x)$ is the density of the struck parton in the incoming proton. However when approaching the kinematic limit where the values of $q(x)$ are very small, the coupling strengths which can be probed with the actual integrated luminosities are too high for the NWA to be valid. The convolution of the steeply falling $q(x)$ with the Breit-Wigner distribution of finite width characterizing the resonance leads to a strong distortion of the LQ mass peak, and the mass spectrum shows very large tails towards low values. As a result the LQ production cross-section σ_s in the s -channel for M_{LQ} approaching $\sqrt{s_{ep}}$ is considerably larger than σ_{NWA} . The deviation from σ_{NWA} is significant (typically $> 10\%$) at $M_{LQ} \gtrsim 250$ GeV for a LQ produced via a valence quark (u, d), and already at $M_{LQ} > 200$ GeV for a production via a sea quark (\bar{u}, \bar{d}) [21]. The analysis presented in the following fully takes into account these effects originating from the finite LQ decay width.

Scalar LQs produced in the s -channel decay isotropically in their rest frame leading to a flat $d\sigma/dy$ spectrum where $y = Q^2/s_{ep}x = \frac{1}{2}(1 + \cos\theta^*)$ is the Bjorken scattering variable in DIS and θ^* is the decay polar angle of

³ The detectors in the backward region were upgraded in 1995 by the replacement of the lead/scintillator calorimeter [20] and a proportional chamber

Table 1. Main properties of the different LQ induced contributions at HERA to $e^+ + q_i \rightarrow l_n^+ + q_j$. For LQs coupling to both eq and $l_n q$ pairs with $l_n \neq e$, β_n denotes the branching ratio of the LQ into $l_n + q_j$. The interference contribution only concerns processes with a first generation lepton in the final state

	Angular Spectrum		Cross-Section	
	y Shape		λ Dependence	
	Scalar	Vector	$M \ll \sqrt{s_{ep}}$	$M \gg \sqrt{s_{ep}}$
s -channel	flat	$(1-y)^2$	$\lambda_{1i}^2 \beta_n$	$\lambda_{1i}^2 \lambda_{nj}^2$
u -channel	$(1-y)^2$	flat	$\lambda_{1i}^2 \lambda_{nj}^2$	$\lambda_{1i}^2 \lambda_{nj}^2$
Interference			λ^2	λ^2

the lepton relative to the incident proton in the LQ centre of mass frame. In contrast, events resulting from the production and decay of vector LQs would be distributed according to $d\sigma/dy \propto (1-y)^2$. These y spectra (or in other words the specific angular distributions of the decay products) from scalar or vector LQ production are markedly different from the $d\sigma/dy \propto y^{-2}$ distribution expected at fixed x for the dominant t -channel photon exchange in neutral current DIS events⁴. Hence, a LQ signal in the NC-like channel will be statistically most prominent at high y .

The u -channel contribution scales with λ^4 . It can compete with resonant production only for LQs with fermion number $|F|=2$ and at high couplings and LQ masses. For $F=0$ LQs, it is highly suppressed by less favorable parton densities as it proceeds via an exchange involving an *anti*quark from the proton. Scalar LQ exchange would lead to events distributed in y according to $d\sigma/dy \sim (1-y)^2$ while vector LQ exchange would lead to a flat y spectrum. However the events originating from u -channel LQ exchange would mainly be concentrated at mass values much lower than M_{LQ} . As such, the kinematic cuts used in this analysis to reduce the number of NC-like and CC-like events (see Sect. 5) also drastically suppress a possible u -channel contribution.

In approaching $M_{LQ} \sim \sqrt{s_{ep}}$, the interference of the LQ s -channel production and u -channel exchange with SM boson exchange can no longer be neglected. This interference can be constructive or destructive⁵ depending on the LQ type. As will be seen in Sect. 6, the set of cuts used in the present analysis focuses on a phase space region where the contribution of the interference is considerably reduced.

⁴ At high momentum transfer, Z^0 exchange is no longer negligible and contributes to less pronounced differences in the y spectra between LQ signal and DIS background

⁵ The signs of the interference terms between SM gauge boson and $F=0$ LQ contributions given in the original BRW paper [9] were found to be incorrect. The correct signs as provided in the *erratum* to [9] have been used here

The experiments at HERA are also sensitive to LQs with $M_{LQ} \gtrsim \sqrt{s_{ep}}$. For first generation LQs, the interference between LQ induced and SM boson exchange processes (which scales with λ^2) generally dominates in this mass range over the s - and u -channel contributions (both scaling with λ^4). For $F=0$ LQs, a nevertheless sizeable s -channel contribution originates from the convolution of the parton density with the low mass tail of the LQ Breit-Wigner resonance of finite width, provided that the coupling λ is not too small. For example, for $\lambda=1$ and for the LQ labelled $S_{1/2,L}$ in the BRW model (see below), the s -channel contribution competes with the interference for M_{LQ} up to $\simeq 400$ GeV, within the kinematic cuts used in Sect. 6.4.

In the cases of $M_{LQ} \gg \sqrt{s_{ep}}$, the propagator entering the LQ amplitudes can be contracted to a four-fermion interaction. One is left with a contact interaction mostly affecting the measured inclusive DIS Q^2 spectrum through interference effects. Constraints on such four-fermion couplings translated into limits on M_{LQ}/λ for first generation LQs will be discussed in a separate paper. For LFV LQs above $\sqrt{s_{ep}}$, both the s - and u -channel contributions may in principle be important for large Yukawa coupling values. There, the LFV LQ cross-sections $\sigma(eq_i \rightarrow l_n q_j)$ (s -channel) and $\sigma(e\bar{q}_j \rightarrow l_n \bar{q}_i)$ (u -channel) only depend on λ_{1i} , λ_{nj} and M_{LQ} via $\lambda_{1i}^2 \lambda_{nj}^2 / M_{LQ}^4$.

Some essential characteristics of the different LQ induced processes contributing at HERA are summarized in Table 1.

The LQ searches will be discussed here either in the strict context of the BRW phenomenological ansatz [9] where the decay branching ratios are fixed by the model, or in the context of generic models allowing for arbitrary branching ratios. The BRW model considers all possible scalar (S_I) and vector (V_I) LQs of weak isospin I with dimensionless couplings $\lambda_{ij}^{L,R}$ to lepton-quark pairs, where L or R is the chirality of the lepton. The general effective Lagrangian which is introduced obeys the symmetries of the SM. There are 10 different LQ isospin multiplets, with couplings to left or right handed fermions, among which there are 5 isospin families of scalar LQs. These are listed in Table 2. We restrict the search to pure chiral couplings of the LQs given that deviations from lepton universality in helicity suppressed pseudoscalar meson decays have not been observed [22,23]. This restriction to couplings with either left- (λ^L) or right-handed (λ^R) leptons (i.e. $\lambda^L \cdot \lambda^R \sim 0$), affects only two scalar (S_0 and $S_{1/2}$) and two vector ($V_{1/2}$ and V_0) LQs. We make use of the so-called Aachen nomenclature and classification scheme [24] and do not use specific symbols to label the *anti*-leptoquarks which are actually produced in e^+p collisions. We make the simplifying assumptions that one of the LQ multiplets is produced dominantly and that the mass eigenstates within the LQ isospin doublets and triplets are degenerate in mass.

For the determination of LQ signal detection efficiencies, we make use of the LEGO event generator [25] and of a complete simulation of the H1 detector response. LEGO incorporates s - and u -channel LQ exchange pro-

Table 2. Leptoquark isospin families in the Buchmüller-Rückl-Wyler model. For each leptoquark, the superscript corresponds to its electric charge, while the subscript denotes its weak isospin. For simplicity, the leptoquarks are conventionally indexed with the chirality of the incoming *electron* which could allow their production in e^-p collisions, e.g. the \tilde{S}_0 will be denoted by $\tilde{S}_{0,R}$ (see text). β_e denotes the branching ratio of the LQ into $e^+ + q$

$F = -2$	Prod./Decay	β_e	$F = 0$	Prod./Decay	β_e
Scalar Leptoquarks					
$^{1/3}S_0$	$e_R^+ \bar{u}_R \rightarrow e^+ \bar{u}$	1/2	$^{5/3}S_{1/2}$	$e_R^+ u_R \rightarrow e^+ u$	1
	$e_L^+ \bar{u}_L \rightarrow e^+ \bar{u}$	1		$e_L^+ u_L \rightarrow e^+ u$	1
$^{4/3}\tilde{S}_0$	$e_L^+ \bar{d}_L \rightarrow e^+ \bar{d}$	1	$^{2/3}S_{1/2}$	$e_L^+ d_L \rightarrow e^+ d$	1
$^{4/3}S_1$	$e_R^+ \bar{d}_R \rightarrow e^+ \bar{d}$	1	$^{2/3}\tilde{S}_{1/2}$	$e_R^+ d_R \rightarrow e^+ d$	1
$^{1/3}S_1$	$e_R^+ \bar{u}_R \rightarrow e^+ \bar{u}$	1/2			
Vector Leptoquarks					
$^{4/3}V_{1/2}$	$e_L^+ \bar{d}_R \rightarrow e^+ \bar{d}$	1	$^{2/3}V_0$	$e_L^+ d_R \rightarrow e^+ d$	1
	$e_R^+ \bar{d}_L \rightarrow e^+ \bar{d}$	1		$e_R^+ d_L \rightarrow e^+ d$	1/2
$^{1/3}V_{1/2}$	$e_L^+ \bar{u}_R \rightarrow e^+ \bar{u}$	1	$^{5/3}\tilde{V}_0$	$e_L^+ u_R \rightarrow e^+ u$	1
$^{1/3}\tilde{V}_{1/2}$	$e_R^+ \bar{u}_L \rightarrow e^+ \bar{u}$	1	$^{5/3}V_1$	$e_R^+ u_L \rightarrow e^+ u$	1
			$^{2/3}V_1$	$e_R^+ d_L \rightarrow e^+ d$	1/2

cesses depicted in Fig. 1b,c. It takes into account initial state QED radiation in the collinear approximation. The parton showers approach [26] relying on the DGLAP [27] evolution equations is used to simulate QCD corrections in the initial and final states, and the kinematics at the decay vertex is properly corrected for effects of the parton shower masses. The non-perturbative part of the hadronization is simulated using string fragmentation [26]. The Mandelstam variable \hat{s} characterizing the $eq \rightarrow lq$ subprocess defines the scale at which the parton density is evaluated as well as the maximum virtuality of parton showers. The LQ signal cross-sections are calculated using the full matrix elements given in [9] and taking into account the contributions from the s - and u -channels as well as the interference with SM boson exchange. The resulting cross-sections are further corrected to account for next-to-leading order (NLO) QCD effects making use of multiplicative K -factors [28] in a procedure described in detail in Sect. 6.4. These NLO QCD corrections which depend on the LQ signal shape expected for a given M_{LQ} and λ are typically of $\mathcal{O}(10\%)$. For the parton densities, use is made of the recent Martin-Roberts-Stirling-Thorne MRST [29] parametrization which better describes existing measurements constraining the sea quark densities in the proton [30,31].

The theoretical uncertainty on the signal cross-section originating mainly from contributions of parton density distributions extracted from “QCD fits” and the value of

the strong coupling constant α_S is treated as a systematic error. This uncertainty is $\simeq 7\%$ for leptoquarks coupling to e^+u , and varies between $\simeq 7\%$ at low LQ masses up to $\simeq 30\%$ around 250 GeV for leptoquarks coupling to e^+d . Above 250 GeV, for coupling values corresponding to the expected sensitivity, the small but finite width of the resonance results in the fact that mainly relatively low x partons are involved in the LQ production. Hence the uncertainty on the signal cross-section decreases for $F = 0$ LQs to $\simeq 7\%$ between 250 GeV and the kinematic limit. For $|F| = 2$ leptoquarks, this uncertainty ranges from $\simeq 10\%$ at low masses and reaches $\simeq 40\%$ around 200 GeV, and then goes down to $\simeq 15\%$ at the kinematic limit. Moreover, choosing alternatively Q^2 or the square of the transverse momentum of the final state lepton instead of \hat{s} as the hard scale at which the parton distributions are estimated yields an additional uncertainty of $\pm 7\%$ on the signal cross-section.

4 Deep inelastic scattering and other background sources

The calculation of the SM expectation for NC and CC DIS ep scattering is performed using the parton model in the approximation of single γ/Z and W boson exchange, and relies on a description of the proton in terms of scale dependent structure functions. The structure functions are expressed in terms of parton densities and are taken here from the MRST parametrization which includes constraints from HERA data up to $Q^2 = 5000 \text{ GeV}^2$ [32, 33]. The parton densities are evolved to the high Q^2 domain relevant for this analysis using the next-to-leading order DGLAP equations. The Monte Carlo event generator DJANGO [34] which follows such an approach is used for the comparison with data. This generator includes the QED first order radiative corrections [35] and a modelling of the emission of QCD radiation via ARIADNE [36]. The ARIADNE generator makes use of the Colour Dipole Model [37] to simulate QCD radiation to all orders and string fragmentation to generate the hadronic final state.

The contributions from all background processes which could give rise to events with true or misidentified isolated leptons at high transverse energy or to events with a large missing transverse momentum have been evaluated. In particular, direct and resolved photoproduction processes were modelled using the PYTHIA generator [38]. It is based on leading order QCD matrix elements and includes initial and final state parton showers calculated in the leading logarithm approximation, and string fragmentation. The renormalization and factorization scales were both set to P_T^2 , P_T being the transverse momentum of the jets emerging out of the hard subprocess. The GRV (G) leading order parton densities in the proton (photon) have been used [39]. The production of electroweak vector bosons Z^0 and W^\pm was modelled using the EPVEC [40] event generator. Contributions from two-photon processes where one γ originates from the proton were also considered and estimated using the LPAIR [41]

event generator. A complete Monte Carlo simulation of the H1 detector response has been performed for all background processes.

The following experimental errors are propagated as systematic errors on the mean SM expectations :

- the uncertainty on the integrated luminosity ($\pm 1.5\%$);
- the uncertainty on the absolute calibration of the calorimeters for electromagnetic energies, ranging between $\pm 0.7\%$ in the central LAr wheels to $\pm 3\%$ in the forward region of the LAr calorimeter (see Sect. 2);
- the uncertainty on the calibration of the calorimeters for hadronic showers of $\pm 2\%$ (see Sect. 2).

In addition, a 7% theoretical uncertainty on the predicted NC DIS cross-section originates mainly from the lack of knowledge on the proton structure (see detailed discussion in [5]) and, to a lesser extent, from the higher order QED corrections. For CC DIS processes which are mainly induced by d quarks, this uncertainty varies with Q^2 and ranges between 7% and $\simeq 20\%$ at the highest Q^2 considered here. All analyses described in the following sections have been repeated with an independent shift of the central values by ± 1 standard deviation of each of the experimental and theoretical sources of errors. The overall systematic error of the SM prediction is determined as the quadratic sum of the resulting errors and of the statistical error on the Monte Carlo simulation.

5 Event selection and comparison with standard model expectation

The search for first generation LQs relies essentially on an inclusive NC selection requiring an identified positron at high transverse energy, and an inclusive CC selection requiring a large missing transverse momentum. The selection of NC- and CC-like events will be described in Subsects. 5.1 and 5.2 respectively where the resulting samples will be compared to SM expectations. For LQs possessing couplings to mixed fermion generations, the selection of $e^+p \rightarrow \mu^+ + q + X$ and $e^+p \rightarrow \tau^+ + q + X$ candidates which will be discussed in Subsects. 5.3 and 5.4 respectively, requires essentially an identified μ or τ lepton together with a large amount of hadronic transverse energy.

In common for all channels analysed, the events must have been accepted by a LAr trigger asking either for an electromagnetic cluster, for a large transverse energy in the central part of the calorimeter, or for a large imbalance in the transverse energy flow. The rejection of background from cosmic rays and from “halo” muons associated with the proton beam mainly relies on constraints on the event timing relative to the nominal time of the beam bunch crossings. Beam-wall and beam-residual gas interactions are furthermore suppressed by requiring a primary vertex in the range $|z - \bar{z}| < 40$ cm where \bar{z} varies within ± 5 cm around $z = 0$ depending on the HERA beam settings.

In what follows, unless explicitly stated otherwise, the energy flow summations run over all energy deposits i in the calorimeters (apart from the electron and photon taggers). Thus, the missing transverse momentum $P_{T,miss}$ is

obtained as

$$P_{T,miss} \equiv \sqrt{\left(\sum E_{x,i}\right)^2 + \left(\sum E_{y,i}\right)^2}$$

with $E_{x,i} = E_i \sin \theta_i \cos \phi_i$ and $E_{y,i} = E_i \sin \theta_i \sin \phi_i$. The momentum balance with respect to the incident positron is obtained as $\sum (E - P_z) \equiv \sum (E_i - E_{z,i})$ with $E_{z,i} = E_i \cos \theta_i$.

5.1 Neutral current deep-inelastic-like signatures

5.1.1 Event selection and kinematics

The **selection of NC DIS-like events** uses mainly calorimetric information for electron finding and energy-momentum conservation requirements, with selection cuts similar to those considered in previous high Q^2 analysis [5]:

1. an isolated positron with $E_{T,e} > 15$ GeV ($E_{T,e} = E_e \sin \theta_e$), found within the polar angular range $5^\circ \leq \theta_e \leq 145^\circ$; the positron energy cluster should contain more than 98% of the LAr energy found within a pseudorapidity-azimuthal cone of opening $\sqrt{(\Delta \eta_e)^2 + (\Delta \phi_e)^2} = 0.25$ where $\eta_e = -\ln \tan \frac{\theta_e}{2}$; at least one charged track is required within the positron isolation cone;
2. a total transverse momentum balance $P_{T,miss} / \sqrt{E_{T,e}} \leq 4\sqrt{\text{GeV}}$;
3. a limited reconstructed momentum loss in the direction of the incident positron such that $40 \text{ GeV} \leq \sum (E - P_z) \leq 70 \text{ GeV}$.

The identification of positron induced showers relies on the detailed knowledge of the expected lateral and longitudinal shower properties [16,18]. The efficiency for the detection of positrons exceeds 90% everywhere within the acceptance cuts, the main losses being due to showers developing through the inactive material between calorimeter modules. The cut (2) makes possible a very efficient NC DIS selection up to the highest Q^2 by taking into account the natural dependence of the calorimetric energy resolution, $E_{T,e}$ being used as an estimate of the scale relevant for the actual $P_{T,miss}$ measurement. The cut (3) retains more than 90% of NC DIS events and exploits the fact that by energy-momentum conservation, the $\sum (E - P_z)$ distribution for NC DIS events is peaked at $2E_e^0$, where E_e^0 is the positron beam energy. It rejects events where a very hard collinear γ is emitted by the initial state positron. To ensure a good control of the positron identification performances, a fiducial cut is applied requiring:

4. an azimuthal impact of the track associated to the positron at $|\phi_e - \phi_{crack}| > 1^\circ$ from the nearest projective ϕ crack in the transverse plane.

The DIS Lorentz invariants Q^2, y and M are determined using only the measurement of the “scattered” positron energy and angle as soon as $|\phi_e - \phi_{crack}| > 2^\circ$,

such that the measurement of E_e is reliable:

$$M_e = \sqrt{\frac{Q_e^2}{y_e}}, \quad Q_e^2 = \frac{E_{T,e}^2}{1 - y_e}, \quad y_e = 1 - \frac{E_e - E_e \cos \theta_e}{2E_e^0}.$$

This method will henceforth be called the electron method (*e*-method). In $\sim 4\%$ of the acceptance corresponding to the range $1^\circ < |\phi_e - \phi_{crack}| < 2^\circ$ where calorimetry measurements of positrons deteriorate, the reconstructed positron energy is corrected to the value given by the double angle method [42]:

$$E_{2\alpha} = \frac{2E_e^0}{\alpha_e + \alpha_h} \frac{1}{\sin \theta_e},$$

using

$$\alpha_e = \tan(\theta_e/2) = \frac{E_e - E_{z,e}}{E_{T,e}}$$

and

$$\alpha_h = \tan(\theta_h/2) = \frac{\sum_h (E - P_z)}{\sqrt{(\sum_h E_x)^2 + (\sum_h E_y)^2}},$$

where the summations run over all energy deposits of the hadronic final state.

In the following analysis, the comparison with SM expectation is restricted to the kinematic range $Q^2 > 2500 \text{ GeV}^2$ and $0.1 < y < 0.9$. The resolution in M_e degrades with decreasing y_e ($\delta M_e/M_e \propto 1/y_e$) and so the low y domain is excluded. Excluding the high y values avoids the region where migrations effects due to QED radiation in the initial state are largest for the *e*-method. In the kinematic range considered and given cuts (1) to (4), the NC trigger efficiency exceeds 98% and is consistent with 100% to within experimental error.

The $y < 0.9$ restriction also suppresses the photoproduction background where e.g. a jet has been misidentified as an electron. Following [5], any possibly remaining non-DIS contamination coming for example from $\gamma\gamma$ or QED Compton processes as well as the background from misidentified low Q^2 NC DIS are further suppressed through a minimal set of specific cuts [18]. Among these a prominent one against multi-lepton final states is the requirement of at least one reconstructed jet with $E_{T,jet} > 7 \text{ GeV}$ found using a cone algorithm in the laboratory frame, with a radius $\sqrt{(\Delta\eta)^2 + (\Delta\phi)^2} = 1$. The jet should be in the polar angular range $7^\circ \leq \theta_{jet} \leq 145^\circ$, and at least 5% of its energy should be deposited in the hadronic section of the LAr calorimeter. Against photoproduction and low Q^2 NC DIS, it is also required that there be less than 7.5 GeV in the backward calorimeter. The specific reduction of the background contamination induces only small ($< 5\%$) efficiency loss for high Q^2 NC DIS-like processes. The remaining contamination is estimated to be below 0.15% and is henceforth neglected.

Leptoquark signal selection efficiencies are determined over a coupling-mass grid with steps in mass of 25 GeV and for coupling values corresponding roughly to the expected sensitivity to properly take into account the effect

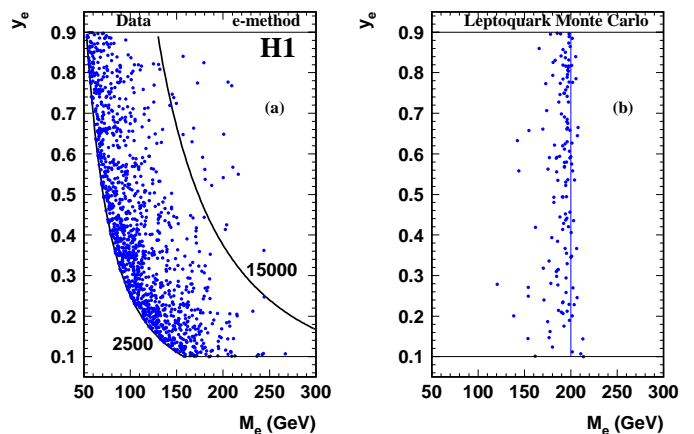


Fig. 2a,b. Kinematics in the $y_e - M_e$ plane of (a) the selected NC DIS candidate events from H1 data (two isocurves at $Q^2 = 2500$ and 15000 GeV^2 are plotted as full lines); (b) a scalar $F = 0$ leptoquark of mass $M_{LQ} = 200 \text{ GeV}$ decaying into $e + q$, for a coupling $\lambda = 0.05$

of the intrinsic finite width of the searched resonance. Detailed Monte Carlo simulation of about 500 events per point on the grid is performed followed by the application of the full analysis chain. The above set of cuts ensures a typical selection efficiency for $LQ \rightarrow e + q$ events which varies between $\simeq 40\%$ and $\simeq 75\%$ for LQ masses ranging in 75 to 250 GeV.

Applying all the above NC selection criteria, 1298 DIS event candidates are accepted which is in good agreement with the expectation of 1243 ± 95 events from standard NC DIS.

5.1.2 Comparison with standard model expectation

Figure 2a shows the distribution of the NC candidates in the $y_e - M_e$ kinematic plane. In such a plane, the signal of a 200 GeV scalar LQ with $F = 0$ could manifest as illustrated in Fig. 2b, for coupling values corresponding to the expected sensitivity. Compared to other commonly used kinematic methods for NC DIS at HERA [10], the *e*-method provides the best peak resolution (truncated Gaussian fit) in mass at high y , where a LQ signal would be most prominent. This resolution on M_e varies within $\simeq 3 - 6 \text{ GeV}$ for LQ masses ranging between 100 and 250 GeV. It should be noted, as can be inferred from Fig. 2b, that the *e*-method underestimates on average the true LQ mass by $\simeq 2\%$ due to migrations caused by final state QCD radiation.

A differential analysis in the $y_e - M_e$ plane of the very high Q^2 events from the 1994 to 1996 datasets [5] had revealed a noteworthy excess of NC DIS-like events at $Q^2 \gtrsim 15000 \text{ GeV}^2$ or for $y_e > 0.4$ at masses $M_e \simeq 200 \text{ GeV}$. A comparison of the measured M , y and Q^2 spectra with standard DIS model expectations can now be re-examined with higher statistics.

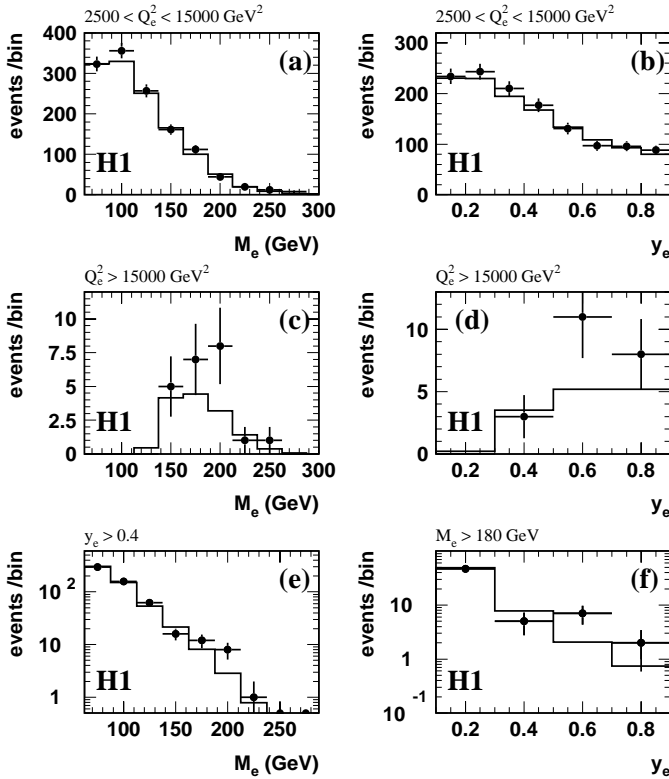


Fig. 3a–f. Distributions of M_e and y_e for the selected NC DIS candidate events, (a) and (b) for $2500 < Q_e^2 < 15000 \text{ GeV}^2$, (c) and (d) for $Q_e^2 > 15000 \text{ GeV}^2$; distributions of (e) M_e for $y_e > 0.4$ and (f) y_e for $M_e > 180 \text{ GeV}$; superimposed on the data points (\bullet symbols) are histograms of the standard NC DIS expectation

We first consider the M_e and y_e information. The projected M_e and y_e spectra are shown in Fig. 3 in several kinematic domains. Figures 3a and 3b show the projected M_e and y_e distributions of the NC DIS-like selected events at “moderate” Q^2 ($2500 < Q_e^2 < 15000 \text{ GeV}^2$) and Fig. 3c and 3d at “very high” Q^2 ($Q_e^2 > 15000 \text{ GeV}^2$). The distributions of the measured data are well reproduced by standard DIS predictions in the low Q^2 range. At high Q^2 the data slightly exceed the NC DIS expectation at $M_e \sim 200 \text{ GeV}$ as can be seen in Fig. 3c. Moreover, Fig. 3d shows that the excess of observed events is more prominent at high y_e , so that at high M_e and large y_e the experiment tends to exceed the SM expectation.

Figure 3e shows the measured and expected M_e distributions for a minimum y_e value of $y_{min} = 0.4$. An excess of events over the NC DIS expectation at high mass ($\sim 200 \text{ GeV}$) is still visible. In the mass range $200 \text{ GeV} \pm \Delta M/2$ with $\Delta M = 25 \text{ GeV}$, $N_{obs} = 8$ events are observed for an expectation of $N_{DIS} = 2.87 \pm 0.48$. The mean mass value of these 8 events as determined with the e -method $\langle M_e \rangle = 202.5 \pm 7.0 \text{ GeV}$ (RMS) agrees within 1.4% with the one obtained from the invariant mass of the final e -jet pairs. Of the observed events, 5 originate from the 1994 to 1996 data (40.3% of \mathcal{L}) and 3 from the 1997 data (59.7%

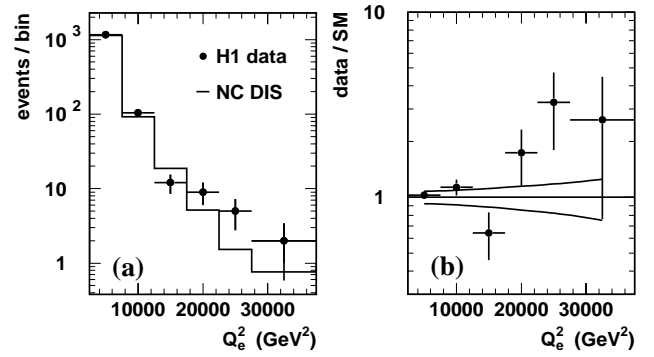


Fig. 4. (a) Q_e^2 distribution of the selected NC DIS candidate events for the data (\bullet symbols) and for standard NC DIS expectation (histogram); (b) ratio of the observed and expected (from NC DIS) number of events as a function of Q_e^2 ; the lines above and below unity specify the $\pm 1\sigma$ levels determined using the combination of statistical and systematic errors of the DIS expectation

of \mathcal{L}). It should be emphasized here that N_{obs} and N_{DIS} are quoted for the same $\Delta M - \Delta y$ region where the most significant excess was observed in the original analysis of the 1994 to 1996 data [5] despite the fact that the individual events are slightly (within originally estimated systematic errors) displaced in the $M - y$ plane. In this domain, 7 events were reported in [5]. These events are measured here at M_e values on average 2.4% higher due to the new *in situ* calibration of the electromagnetic section of the LAr calorimeter, and thus, one event has now migrated outside this ΔM domain. The estimated mass of one of the other 6 events in which the positron lies within less than 2° from the closest ϕ crack was and remains measured outside this mass region when using the double angle method in contrast to the e -method used in [5]. It was explicitly checked that repeating the 1994 to 1996 analysis procedures of [5] but using this new calibration leaves the statistical significance and the physics messages of [5] unchanged.

At large mass $M_e > 180 \text{ GeV}$ and for $y_e > 0.4$, we observe in the 1994 to 1996 data $N_{obs} = 7$ in slight excess of the expectation of $N_{DIS} = 2.21 \pm 0.33$ while in the 1997 data alone $N_{obs} = 4$ events are observed, in good agreement with the expectation of $N_{DIS} = 3.27 \pm 0.49$. The y_e distribution of these high mass events is shown in Fig. 3f.

Hence, no significant excess is seen in the mass spectrum for the 1997 data alone and the “clustering” around $M_e \sim 200 \text{ GeV}$ is, overall, thus rendered less significant than that observed with 1994 to 1996 data only.

We then consider the Q^2 information. Figure 4a shows the measured Q_e^2 distribution in comparison with the expectation from standard NC DIS processes. Also shown in Fig. 4b is the ratio of the observed Q_e^2 distribution to the NC DIS expectation. The errors resulting from the convolution of the systematic errors and the statistical error of the Monte Carlo sample are correlated for different Q_e^2 bins and are indicated in Fig. 4b as lines above and below

unity joining the $\pm 1\sigma$ errors evaluated at the centre of each bin. These errors are dominated by the uncertainty in the electromagnetic energy scale of the calorimeter and vary between 7.7% at low Q_e^2 and 25% at the highest values of Q_e^2 . The NC DIS expectation agrees well with the data for $Q_e^2 \lesssim 10000 \text{ GeV}^2$ while at larger Q_e^2 , deviations are observed, with a slight deficit around 15000 GeV^2 and a number of observed events at $Q^2 \gtrsim 15000 \text{ GeV}^2$ in excess of the NC DIS expectation. For $Q^2 > 15000 \text{ GeV}^2$, 22 events are observed while 14.1 ± 2.0 are expected from standard NC DIS.

5.2 Charged current deep-inelastic-like signatures

5.2.1 Event selection and kinematics

The inclusive selection of CC DIS-like events requires:

1. no e^\pm candidate with $E_T > 5 \text{ GeV}$ found in the LAr calorimeter;
2. the total missing transverse momentum $P_{T,miss} > 30 \text{ GeV}$.

These cuts eliminate the photoproduction and NC DIS background. To deal with specific background sources to CC DIS, it is required that there be no isolated track with $P_T > 10 \text{ GeV}$ found within the angular range $10^\circ \leq \theta \leq 145^\circ$. This reduces the remaining contamination to $< 0.3\%$ from misidentified NC DIS events where the positron has been scattered through a crack of the calorimeter and also suppresses eventual background from single W boson, while causing negligible efficiency losses for the CC DIS selection.

The Q^2 , y and M are calculated using the Jacquet-Blondel ansatz [43] by summing over all measured final state hadronic energy deposits using:

$$M_h = \sqrt{\frac{Q_h^2}{y_h}}, \quad Q_h^2 = \frac{P_{T,miss}^2}{1 - y_h}, \quad y_h = \frac{\sum (E - P_z)}{2E_e^0}.$$

This method will henceforth be called the hadron method (h -method).

In addition to the cuts (1) and (2) above, the analysis is restricted to the kinematic domain $Q_h^2 > 2500 \text{ GeV}^2$ and $y_h < 0.9$. The resolutions in both M_h and Q_h^2 degrade with increasing y since both $\delta M_h/M_h$ and $\delta Q_h^2/Q_h^2$ behave as $1/(1 - y_h)$ for $y_h \sim 1$. Hence the high y_h domain is excluded. Throughout the remaining domain, the CC trigger efficiency is $96.5 \pm 2\%$. For $LQ \rightarrow \nu + q$ events, these selection criteria ensure typical efficiencies varying between $\simeq 32\%$ and $\simeq 79\%$ for LQ masses ranging in 75 to 250 GeV.

Following this CC selection, 213 DIS event candidates are accepted in good agreement with the standard CC DIS expectation of 199.1 ± 11.5 events.

5.2.2 Comparison with standard model expectation

Figure 5a shows the two dimensional distribution of y_h against M_h for the CC candidates. Signal Monte Carlo

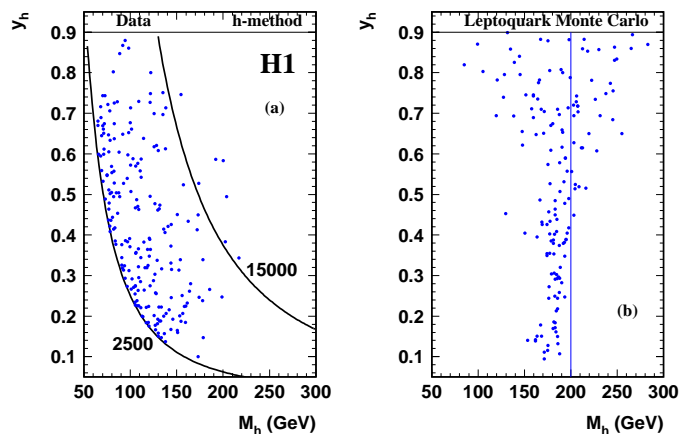


Fig. 5a,b. Kinematics in the $y_h - M_h$ plane of (a) the selected CC DIS candidate events from H1 data (two isocurves at $Q^2 = 2500$ and 15000 GeV^2 are plotted as full lines); (b) a scalar leptoquark resonance of mass $M_{LQ} = 200 \text{ GeV}$ decaying into $\nu + q$, for a coupling $\lambda = 0.05$

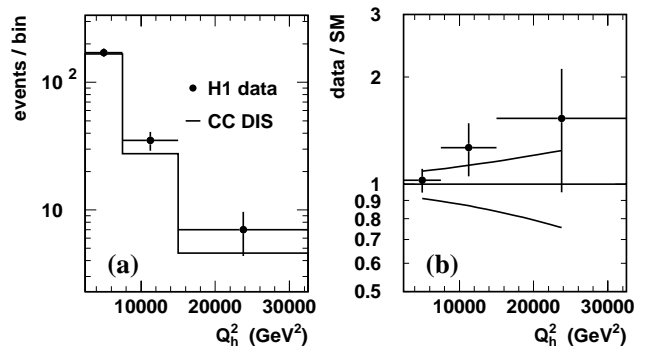


Fig. 6. (a) Q_h^2 distribution of the selected CC DIS candidate events for the data (\bullet symbols) and for standard CC DIS expectation (histogram); (b) ratio of the observed and expected (from CC DIS) number of events as a function of Q_h^2 ; the lines above and below unity specify the $\pm 1\sigma$ levels determined using the combination of statistical and systematic errors of the DIS expectation

events coming from the decay of a 200 GeV narrow scalar resonance into $\nu + q$ are shown in the same plane in Fig. 5b, where the degradation of the resolution in M_h at high y_h is clearly visible. This resolution on the LQ mass is of about 10%. While the relative calibration of the hadronic scale is known at the 2% level (as discussed in Sect. 2 and controlled comparing real and simulated NC DIS events), the energy scale procedure which relies on transverse momentum balance does not attempt to correct on average in DIS events the measured M_h to a “true” value. The measured M_h underestimates the resonance mass systematically by $\simeq 6\%$ and this shift will be taken into account in deriving LQ results.

Figures 6a and 6b show for the CC selection the measured Q_h^2 distribution in comparison with the standard CC DIS expectation. As can be seen in Fig. 6b, the sys-

tematic errors are relatively large and dominated by the uncertainty on the hadronic energy scale of the calorimeter. In the kinematic region $Q_h^2 > 15000 \text{ GeV}^2$, there are $N_{obs} = 7$ observed events compared with an expectation of 4.84 ± 1.42 from standard CC DIS.

5.3 High P_T muon signatures

For LQs possessing a coupling to a second generation lepton, leading to $\mu + q$ final states, we start from a CC-like selection in the kinematic domain $Q_h^2 > 1000 \text{ GeV}^2$ and $P_{T,miss} > 25 \text{ GeV}$, and then require:

1. an identified isolated muon with transverse momentum $P_{T,\mu} > 10 \text{ GeV}$ and within polar angular range $10^\circ < \theta_\mu < 145^\circ$, where the momentum and angle are determined by the associated track. There should be no other charged track linked to the primary interaction vertex within the pseudorapidity-azimuthal isolation cone centred on the μ track of opening $\sqrt{(\Delta\eta_\mu)^2 + (\Delta\phi_\mu)^2} = 0.5$;
2. at least one jet found in the angular range $7^\circ < \theta < 145^\circ$, with a transverse momentum $P_T > 15 \text{ GeV}$, using the cone algorithm mentioned in 5.1.1.

The muon identification combines inner tracking and calorimetric information. Within the μ isolation cone, at least 1 GeV must be visible in the calorimeters. Restricting to the LAr calorimeter, this energy should be smaller than one third of the μ track momentum. Less than 5 GeV should be seen in the conical envelope between $0.5 < \sqrt{(\Delta\eta_\mu)^2 + (\Delta\phi_\mu)^2} < 1.0$. The centroid of the energy deposits in the calorimeters within the μ isolation cone should not be in the LAr electromagnetic section. With these identification criteria, muons are found with a typical efficiency of $\simeq 85\%$ over most of the angular range.

Only four $\mu + jet$ events are observed after applying these basic requirements. These four “outstanding” events are amongst⁶ the high P_T lepton events discussed in [44]. With these selection criteria 0.60 ± 0.10 events are expected from SM processes, coming mainly from W production and inelastic photon-photon interactions $\gamma\gamma \rightarrow \mu^+\mu^-$.

For the $2 \rightarrow 2$ body LQ induced processes, where the final state consists of only the muon and the scattered quark, the energy-momentum conservation relates the polar angle θ_l of the muon to the measurement of the hadronic final state, by :

$$\tan \frac{\theta_l}{2} = \frac{2E_e^0 - \sum(E - p_z)}{\sqrt{(\sum E_x)^2 + (\sum E_y)^2}}.$$

The selection of $\mu + jet$ candidates induced by LQ decay or u -channel exchange requires that :

- (i) the polar angle θ_μ of the high P_T isolated track agrees with θ_l within 30° ;

⁶ The event labelled μ_3 in [44], in which both an isolated muon and the scattered positron are identified, does not fulfil the first requirement (see Sect. 5.2.1) we apply to select CC-like events

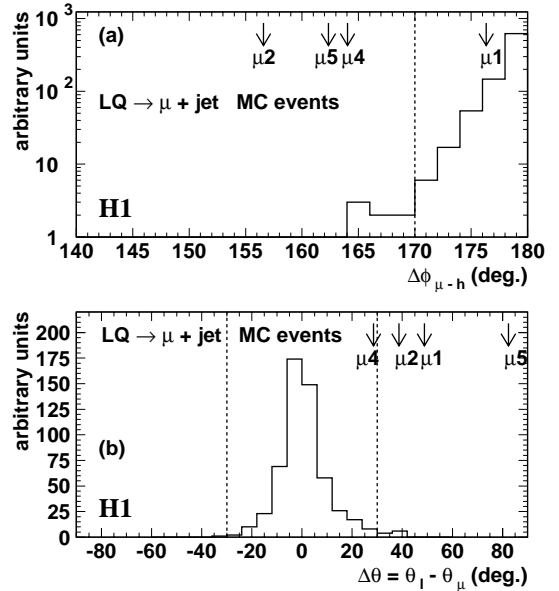


Fig. 7. (a) Azimuthal opening between the track associated to the high P_T muon in $e+p \rightarrow \mu + jet$ events and the hadronic energy flow; (b) polar angle opening between the muon track and the final state lepton angle predicted from the hadronic energy flow for a $2 \rightarrow 2$ body process. Arrows indicate the $\Delta\phi$ and $\Delta\theta$ values for the “outstanding” events reported in [44] and labelled as therein. Histograms represent the expected distributions of these variables for $eq \rightarrow \mu q'$ LQ Monte Carlo events

- (ii) the track and the hadronic flow are back-to-back ($\Delta\phi_{\mu-h} > 170^\circ$) in the plane transverse to the beam axis.

As seen in Fig. 7, these criteria induce a minute efficiency loss for a LQ signal simulation. The actual loss was estimated to be $\simeq 5\%$ using real NC-like data by searching for the charged track angles associated with the positron candidate as deduced using the hadronic energy flow. The above requirements lead to typical efficiencies to select $LQ \rightarrow \mu + q$ events which vary between $\simeq 30\%$ and $\simeq 60\%$ for LQ masses ranging in 75-250 GeV. For LQ masses far above the kinematic limit ($M_{LQ} \gg \sqrt{s_{ep}}$), the distribution of the polar angle of the final state lepton depends on the LQ spin and fermion number (this latter affecting the relative contributions of the s - and u -channels). With the above selection criteria the efficiency to select $\mu + jet$ events induced by very heavy LQs varies between $\simeq 20\%$ and $\simeq 33\%$ depending on the LQ quantum numbers, but independently on the LQ mass.

We observe no candidate satisfying the LQ $\mu + jet$ selection while 0.12 ± 0.05 are expected from SM processes (mainly from inelastic photon-photon interactions). In particular, the $e^+p \rightarrow \mu^+X$ outstanding events discussed in [44] fail significantly the kinematic constraints for LQ induced $eq \rightarrow \mu q'$ processes as can be seen in Fig. 7.

5.4 High P_T tau signatures

For LQs possessing a coupling involving a third generation lepton leading to $\tau+q$ final states, the analysis is restricted to hadronic decays of the τ ⁷. The identification of “pencil-like” jets induced by hadronic decays of τ requires that the jet invariant mass satisfies $M_{jet} \leq 7$ GeV and has a low multiplicity, namely $1 \leq N_{tracks} \leq 3$, N_{tracks} being the number of vertex fitted tracks with $P_T > 0.15$ GeV in the jet identification cone. The jet mass M_{jet} is here calculated as the invariant mass of all energy deposits associated to the jet, each of those being treated as a massless object.

Inclusive τ + jet signatures, where the τ lepton decays into hadrons, are selected by requiring that :

1. no e^\pm candidate with $E_T > 5$ GeV is found in the LAr calorimeter;
2. two jets are found in the angular range $7^\circ < \theta < 145^\circ$ using the cone algorithm mentioned in 5.1.1 with a transverse momentum $P_T > 30$ GeV; one of these jets must satisfy the “loose” τ -jet identification criteria described above;
3. there is at most a small amount of energy deposited in the backward calorimeter, $E_{back} < 7.5$ GeV;
4. the impact point of the “leading track” associated to the τ -jet candidate at the inner surface of the LAr calorimeter must be at least 2° apart in azimuth from each of the eight ϕ cracks of the LAr. The “leading track” is, among the vertex fitted tracks found in the jet identification cone, the one which has the highest momentum projected on the jet axis;
5. the leading track associated to the τ -jet candidate carries a large enough fraction $E_{track}/E_{jet} > 10\%$ of the jet energy E_{jet} ;
6. the fraction of the τ -jet candidate energy carried by the leading track and the energy deposition fraction f_{em} in the LAr electromagnetic section of the τ -jet are such that

$$f_{em} + E_{track}/E_{jet} < 1.5 \quad ;$$

7. the energy deposits of the jet should present an important longitudinal dispersion $R_L = \sqrt{\langle l^2 \rangle - \langle l \rangle^2} > 7$ cm where, for each deposit, l is the distance from the impact point at the calorimeter surface along the jet axis;
8. at most two vertex fitted tracks are found in the azimuthal hemisphere containing the τ -jet candidate.

Cuts (1) to (3) ensure a preselection of τ + jet candidate events at high P_T ; low Q^2 NC DIS is suppressed by cut (3). At this stage, 375 events are selected in the data while 365.7 are expected from NC DIS and γp processes. Figure 8a shows, for these selected candidates, the distribution of the polar angle $\theta_{\tau-jet}$ of the τ -jet candidate. Photoproduction background, where a low multiplicity jet

⁷ The $\tau^+ \rightarrow \mu^+ \nu_\mu \bar{\nu}_\tau$ channel is covered implicitly by the above $\mu + q$ search since the τ decay products are strongly boosted in the τ direction; the $\tau^+ \rightarrow e^+ \nu_e \bar{\nu}_\tau$ channel is not covered here

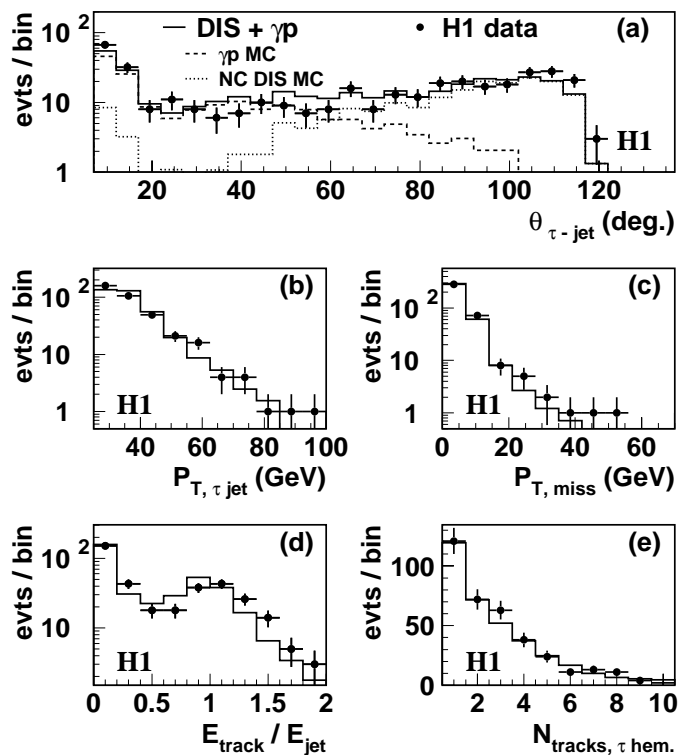


Fig. 8a–e. Distributions of (a) the polar angle $\theta_{\tau-jet}$ of the τ -jet candidate; (b) the transverse momentum of the τ -jet candidate; (c) the total missing transverse momentum; (d) the fraction of the energy of the τ -jet candidate carried by the leading track and (e) the number of tracks in the azimuthal hemisphere containing the τ candidate. Symbols correspond to data events and histograms to SM simulation

can fake a τ -jet, is seen to contribute mainly at low $\theta_{\tau-jet}$ in contrast to NC DIS background arising when the scattered positron has not been identified. NC DIS contamination at low values of $\theta_{\tau-jet}$ is due to events where the positron has been scattered at large angle through a crack of the calorimeter, and where the “current jet” has been identified as a high P_T τ -jet. Figures 8b and c show the distributions of the transverse momentum of the τ -jet and of the whole final state. Figure 8d shows the ratio of the energy of the leading track associated with the τ -jet candidate, to the τ -jet energy. The observed distribution of this fraction E_{track}/E_{jet} is shifted by 9% compared to the one expected from the simulation. This shift is taken into account as a systematic error on the quantity E_{track}/E_{jet} , propagated when estimating the uncertainty on the SM expectation. On Fig. 8e the number of tracks found in the azimuthal hemisphere containing the τ -jet candidate is shown to be well described by the simulation.

NC DIS and γp backgrounds are further reduced by requirements (4) to (8). Cut (4) avoids regions close to ϕ cracks of the calorimeter and hence suppresses NC DIS background. Cut (5) efficiently reduces γp background where a low multiplicity jet could fake a τ -jet. Cut (6) ensures a powerful suppression of the remaining NC DIS

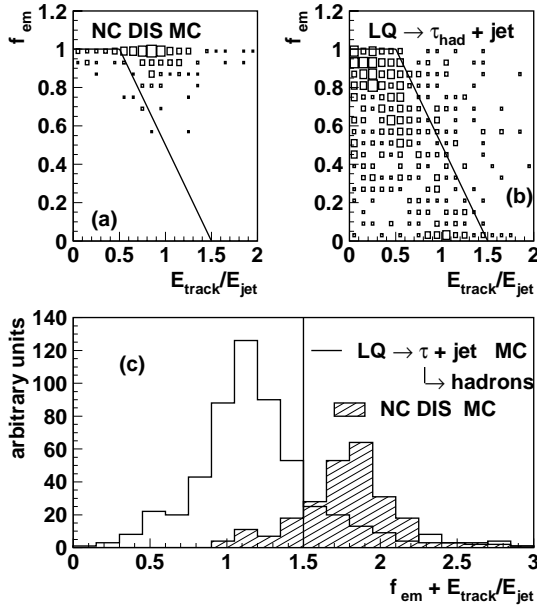


Fig. 9a–c. Correlation between the electromagnetic fraction of the τ -jet candidate and the fraction of the jet energy carried by the leading track for (a) NC DIS and (b) $LQ \rightarrow \tau + q$ simulated events; (c) shows the sum of these variables and the cut applied. Events where the track associated to the τ -jet candidate is at less than 2° in azimuth from a ϕ crack of the calorimeter have been excluded

background events where the scattered positron has not been identified. It exploits the fact that the electromagnetic fraction of a τ -jet is high mainly when the τ lepton decays to $n\pi^0 + X$, which generally implies a small value for the ratio $E_{\text{track}}/E_{\text{jet}}$. On the contrary, for NC DIS events where the positron has been misidentified because its shower has a substantial leakage into the hadronic section of the calorimeter, this ratio $E_{\text{track}}/E_{\text{jet}}$ is expected to peak at one. Figure 9 illustrates this property of τ jets and shows how cut (6) discriminates the searched signal from the DIS background. Remaining NC DIS events are further removed by cut (7). The more stringent requirement on the track multiplicity imposed by cut (8) further reduces the remaining γp contamination. This cut takes into account the fact that two reconstructed tracks can be associated to a single charged particle, especially when scattered in the forward region.

The efficiency to identify τ leptons decaying hadronically using the above criteria is $\simeq 25\%$.

We observe 21 events satisfying the above inclusive $\tau + \text{jet}$ requirements, which agrees well with the mean expectation of 25.4 ± 4.3 events coming from NC DIS and γp processes.

For the $\tau + X$ channel, additional cuts relevant for the specific LQ search are applied :

- (i) a total transverse momentum $P_{T,\text{miss}} > 10$ GeV ;
- (ii) the τ -jet candidate is at $\Delta\phi_{\tau-h} > 160^\circ$ from the total hadronic flow.

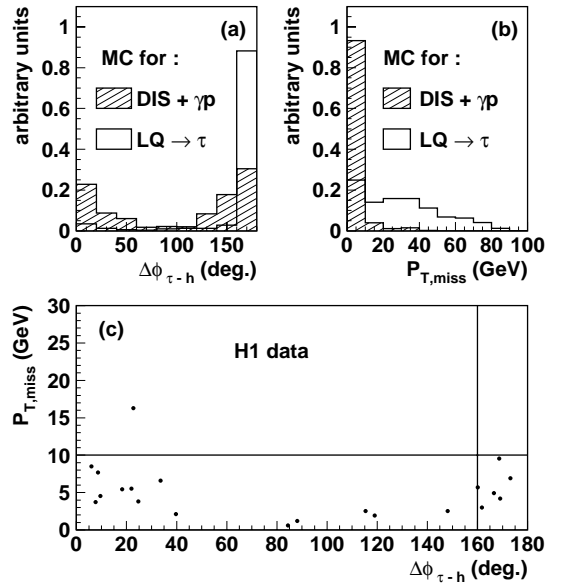


Fig. 10a–c. Distributions of (a) the azimuthal angular opening $\Delta\phi_{\tau-h}$ between the τ -jet candidate and the hadronic energy flow; (b) the missing transverse momentum $P_{T,\text{miss}}$. White and hatched histograms correspond to the SM expectation and the LQ induced $\tau + \text{jet}$ signal respectively. (c) Correlation of these two variables for the data events satisfying cuts (1) to (8). The full lines show the cuts applied, which retain the upper-right part of this plane

Both these cuts exploit the fact that neutrino(s) emerging from the τ decay are collimated with the τ -jet direction, and that the other jet in LQ induced $\tau + \text{jet}$ events is formed by the fragmentation of a quark and thus should not contribute to the missing transverse momentum. Moreover, cut (i) efficiently reduces the remaining NC DIS contamination. The correlation between the $P_{T,\text{miss}}$ and the $\Delta\phi_{\tau-h}$ for the 21 data events which satisfy the criteria (1) to (8) listed above is shown in Fig. 10, together with the expected distributions of $\Delta\phi_{\tau-h}$ and $P_{T,\text{miss}}$ for LQ induced $\tau + \text{jet}$ Monte Carlo events.

The final selection efficiency on the LQ $\tau + q$ signal is $\simeq 10\%$ for LQ masses of 100 GeV and reaches a plateau at $\simeq 25\%$ above 200 GeV. The small efficiency at low masses is mainly due to the requirement of two high P_T jets. For LQ masses far above the kinematic limit, this efficiency varies between $\simeq 8\%$ and $\simeq 12\%$ depending on the LQ spin and fermion number.

We observe no candidate satisfying the additional cuts designed specifically for LQ induced processes involving third generation leptons for an expectation of 0.77 ± 0.30 event from misidentified electrons in NC DIS processes.

It should be noted that the absence of $\tau + \text{jet}$ candidates accompanied by a large $P_{T,\text{miss}}$, despite the relatively loose τ -jet requirements, makes it rather unlikely for the μ 's in the $e^+p \rightarrow \mu^+X$ events [44] to originate from a jet fluctuating in one single particle. Conversely, these muon events fail significantly the kinematic requirements of a two body decay $LQ \rightarrow q + \tau$ followed by a

$\tau \rightarrow \mu^+ \nu_\mu \bar{\nu}_\tau$ decay since the final state μ^+ would appear boosted in the τ direction and the $\Delta\theta$ - $\Delta\phi$ restrictions of Fig. 7 would still apply.

6 Constraints on first generation leptoquarks

6.1 The leptoquark specific angular cut

We first consider LQs possessing couplings to $e-q$ or $e-\bar{q}$ pairs only.

In order to enhance the significance of a possible LQ signal over the NC DIS background remaining after the selection requirements described in Sect. 5.1.1, the specific angular distributions for LQ induced processes are exploited. For scalar or vector LQs with either $F = 0$ or $|F| = 2$, distinct mass dependent lower $y_e > y_{cut}$ cuts have been optimized using Monte Carlo generator programs to maximize the signal significance. This has been achieved by finding the best compromise between the efficiency loss on the LQ signal and the important background reduction. Thus, with increasing LQ mass, the y_{cut} decreases together with the NC DIS expectation. However, for LQ masses close to the kinematic limit, the mass spectrum is highly distorted towards low values (as explained in Sect. 3). Thus, a higher y_{cut} will be needed to enhance the signal significance of such a high mass LQ observed at $M_e \ll M_{LQ}$ where a larger NC DIS background is expected. The evolution of y_{cut} as a function of the LQ mass is represented in Fig. 11a, for the example of $F = 0$ and $|F| = 2$ scalar LQs. For a scalar $F = 0$ LQ, the y_{cut} monotonously decreases from $\simeq 0.6$ around 60 GeV to $\simeq 0.2$ around 260 GeV, and then rises up to $\simeq 0.5$ at 300 GeV. The behaviour is similar for a scalar $|F| = 2$ LQ, but the effect of the distortion of the mass spectrum is significant already at $\simeq 200$ GeV. A similar description holds for vector LQs but smaller values of the y_{cut} are obtained, because of the $(1-y)^2$ shape of their y spectra.

6.2 The mass spectra

The comparison of the measured mass spectrum with SM predictions is shown in Fig. 12a for the NC DIS analysis. The measured and expected NC spectra are seen before and after applying the mass dependent y_e cut relevant for a $F = 0$ scalar LQ. After this y_e cut, we observe 310 events in the mass range $M_e > 62.5$ GeV while 301.2 ± 22.7 are expected. The observed mass spectrum is seen to be well described by the SM expectation, with nevertheless a slight excess in the mass range $200 \text{ GeV} \pm \Delta M/2$ with $\Delta M = 25$ GeV, due to the same 8 events already discussed in Sect. 5.1.2 (the cut optimal for $F = 0$ LQs is $y_{cut} \simeq 0.4$ for $M \simeq 200$ GeV). For CC DIS-like final states, the mass distribution of the 213 events fulfilling the requirements described in Sect. 5.2.1 is seen in Fig. 12b to be in good agreement with the SM prediction.

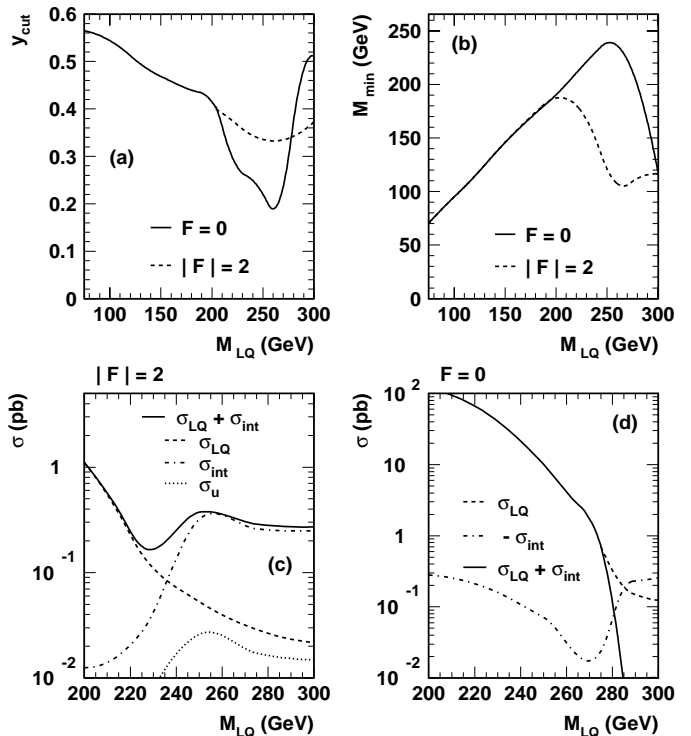


Fig. 11a–d. Lower cut applied (a) on y_e and (b) on M_e to enhance the signal significance for a $F = 0$ (full line) and a $|F| = 2$ (dashed line) scalar leptoquark, for NC DIS-like final states; contribution σ_{LQ} of the LQ induced $e^+p \rightarrow e + q + X$ processes (s - and u -channels summed) and of their interference σ_{int} with SM DIS for (c) $S_{0,R}$ ($|F| = 2$) and (d) $S_{1/2,L}$ ($F = 0$) leptoquark, with $\lambda = 0.5$. In (c), the contribution of the u -channel LQ exchange alone is also represented (dotted line). Each contribution has been integrated over the phase space allowed by the mass dependent M_e and y_e cuts applied in the analysis

6.3 The limits derivation

Assuming that the observed excess of events in the NC DIS-like channel is due to a statistical fluctuation (or either, formally, that the event sample contains at most two components, an unknown LQ signal and a known expectation from NC DIS), models containing first generation leptoquarks can be constrained.

An upper limit N_{lim} on the number of events coming from leptoquark induced processes can be obtained assuming Poisson distributions for the SM background expectation and for the signal. For each contributing channel, we use the numbers of observed and expected events within a mass bin $[M_{min}, M_{max}]$ of variable width, adapted to the expected mass resolution and measured mass values for a given true LQ mass, and which slides over the accessible mass range. For example, only NC DIS (respectively CC DIS) candidates $M_e \in [186; 204]$ GeV ($M_h \in [170; 214]$ GeV) will be used to constrain a 200 GeV LQ undergoing a NC (CC) DIS-like decay. For high LQ masses, the mass bin becomes very large because of the dis-

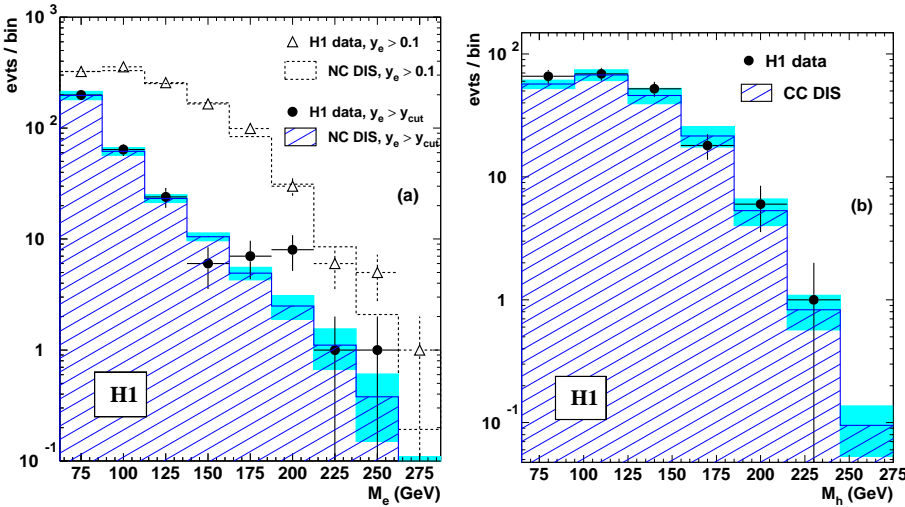


Fig. 12a,b. Mass spectra for (a) NC DIS-like and (b) CC DIS-like final states for data (symbols) and DIS expectation (histograms). In (a), the NC DIS-like comparison is shown before (open triangles, white histogram) and after (closed dots, hatched histogram) a y cut designed to maximize the significance of an eventual scalar LQ signal. The greyed boxes indicate the $\pm 1\sigma$ band combining the statistical and systematic errors of the NC and CC DIS expectations

tortion of the mass spectrum mentioned in Sect. 3. The evolution of M_{min} as a function of the LQ mass is represented in Fig. 11b for $F = 0$ and $|F| = 2$ scalar LQs in the NC-like channel. For LQs undergoing NC DIS-like decays, typical signal detection efficiency including the optimized y and mass cuts is found to vary between 24% at 75 GeV, $\simeq 35\%$ around 200 GeV and 48% at 250 GeV. In the CC DIS-like decay channel, this efficiency ranges between $\simeq 19\%$ for a 75 GeV leptoquark, $\simeq 39\%$ at 100 GeV and reaches 53% at 200 GeV.

In Sect. 6.4, we will consider the BRW model where the only free parameter is the Yukawa coupling λ . Only NC DIS-like data will be used to derive N_{lim} , which can then be translated into an upper limit on $\sigma_{LQ} + \sigma_{int}$, σ_{LQ} being the part of the $e^+p \rightarrow e + q + X$ cross-section induced by the LQ s - and u -channel processes, and σ_{int} the interference term with DIS, both integrated over the phase space allowed by the mass dependent cuts applied in the analysis on M_e and y_e . The evolution of these integrated contributions σ_{LQ} and σ_{int} as a function of the LQ mass is shown in Fig. 11c for the $S_{0,R}$ ($|F| = 2$) scalar leptoquark, as the dashed and dash-dotted lines respectively, and in Fig. 11d for the $S_{1/2,L}$ ($F = 0$), with emphasis on the high mass domain where the interference contribution becomes visible. In the former case the interference between LQ induced processes and SM boson exchange is constructive, while it is destructive for the latter. The cross-sections have here been calculated for a fixed value $\lambda = 0.5$, which is typical for the experimental sensitivity in the displayed mass range. In Fig. 11c the contribution σ_u of the u -channel $S_{0,R}$ exchange alone is also shown as the dotted line (for the case depicted in Fig. 11d, σ_u is below 10^{-4} pb and is not represented in the figure). As was mentioned in Sect. 3, the mass dependent cuts applied on M_e and y_e considerably reduce the contributions of the interference and of virtual exchange (e.g. by a factor $\mathcal{O}(10)$ for a $S_{0,R}$ LQ at $M_{LQ} = 250$ GeV). As can be seen in Fig. 11c and d, the interference is negligible for $F = 0$ leptoquarks and masses up to $\simeq 275$ GeV, but plays an important role

for $|F| = 2$ LQs as soon as $M_{LQ} \simeq 220$ GeV. Moreover the u -channel contribution is always negligible.

In the mass domain where the interference between standard DIS and LQ induced processes can be neglected, we will move away from the BRW model and consider a more general case where the branching $\beta_e = \beta(LQ \rightarrow eq)$ is not determined by λ only. Taking β_e and $\beta_\nu = \beta(LQ \rightarrow \nu q)$ as free parameters, NC and CC DIS-like data can be combined to derive N_{lim} , which can then be translated into an upper limit on the signal cross-section $\sigma_{LQ} = \sigma_s + \sigma_u$ and thus on the Yukawa coupling λ . This will be done in Sect. 6.5. The signal cross-section in the mass domain considered being largely dominated by the s -channel resonant production as mentioned above, an upper limit on $\sigma_s \times \beta_e$ can also be derived. Fixing λ , mass dependent upper limits on the branching ratio β_e can then be obtained, as will be done in Sect. 6.6 using NC DIS data only. In these two cases, we make use of the signal detection efficiencies given above to translate N_{lim} into an upper limit on the signal cross-section.

The procedure which folds in, channel per channel, the statistical and systematic errors is described in detail in [11].

6.4 Mass dependent limits on the Yukawa coupling in the BRW model

We first establish constraints on the BRW model described in Sect. 3 taking into account all LQ induced contributions, but restricting the analysis to NC DIS-like processes. For the decay of resonantly produced LQs, the values of β_e are specified and given in Table 2. As discussed in Sect. 3, the constraints can be extended beyond the kinematic limit by profiting from the tail expected in the s -channel towards low masses, and by properly taking into account the interference with SM boson induced processes.

In the very high mass domain, the interference σ_{int} of LQ induced processes with NC DIS generally dominates

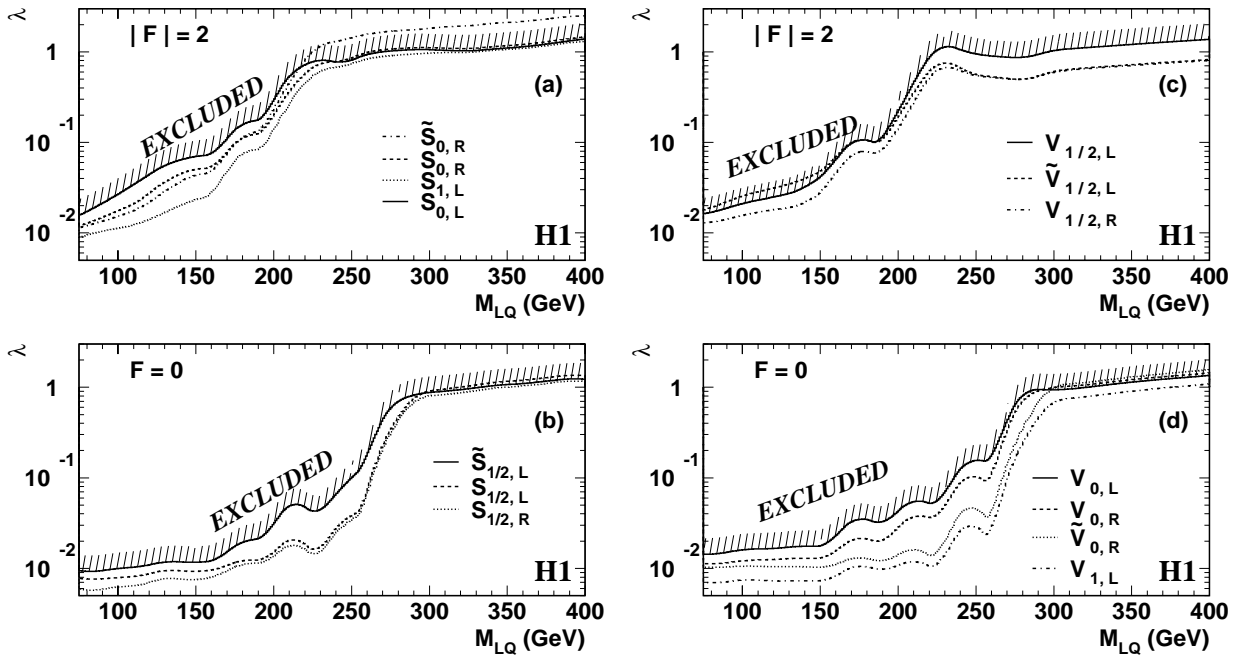


Fig. 13a–d. Exclusion limits at 95% CL on the Yukawa coupling λ as a function of the leptoquark mass for (a) $|F| = 2$ and (b) $F = 0$ scalar, (c) $|F| = 2$ and (d) $F = 0$ vector leptoquarks described by the BRW model. Domains above the curves are excluded

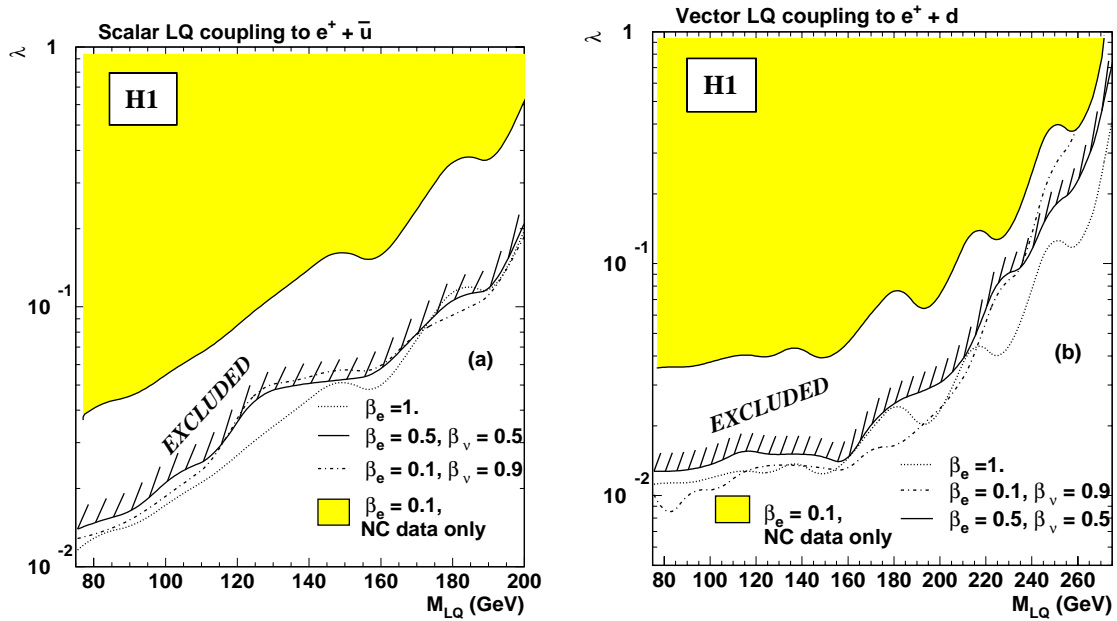


Fig. 14a,b. Exclusion limits at 95% CL on the Yukawa coupling λ as a function of the leptoquark mass for (a) scalar leptoquarks produced via $e^+ \bar{u}$ fusion and (b) vector leptoquarks produced via $e^+ d$ fusion. Different hypotheses for the branching ratios into $eq, \nu q$ are considered. Domains above the curves are excluded

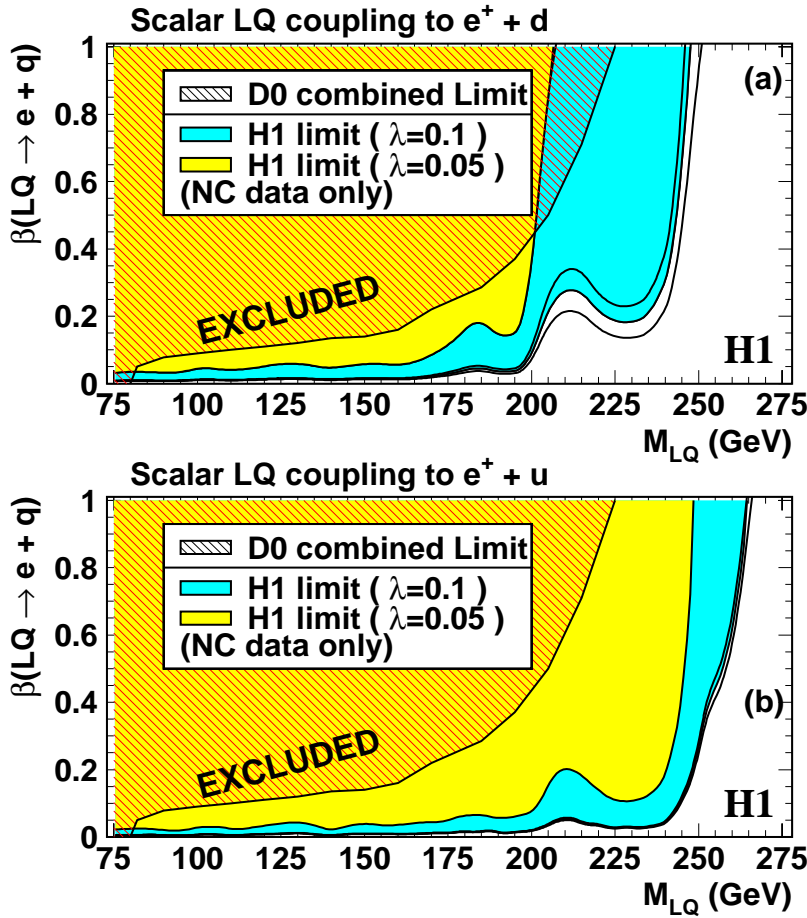


Fig. 15a,b. Mass dependent exclusion limits at 95% CL on the branching ratio $\beta(LQ \rightarrow eq)$ for scalar leptoquarks produced by (a) e^+d and (b) e^+u fusion. Two exclusion regions corresponding to $\lambda = 0.1$ and $\lambda = 0.05$ are represented as greyed areas. For $\lambda = 0.1$, the error bands on the exclusion limits in (a) and (b) illustrate the sensitivity to d and u quark densities respectively (see text). The $D\emptyset$ limit is also shown as hatched region

the LQ cross-section σ_{LQ} . Instead of σ_{LQ} alone, we are thus directly sensitive to $\sigma_{sum} = \sigma_{LQ} + \sigma_{int}$, which, for those LQ species which interfere destructively with DIS, could be negative when integrated over the whole phase space, but remains positive within the kinematic cuts applied. We thus proceed the following way :

- For a given LQ mass M_{LQ} , the numbers of observed and expected events within the optimized cuts $M_{min} < M_e < M_{max}$ and $y_e > y_{cut}$ are used to set an upper limit N_{lim} on the number of signal events. For LQ masses above the kinematic limit, the optimized M_e and y_e cuts are nearly independent of M_{LQ} and close to those displayed in Fig. 11a,b for $M_{LQ} = 300$ GeV. A first estimate λ_0 of the upper limit on λ is then obtained by solving : $N_{lim} = \mathcal{L} \sigma_{sum,cuts}(\lambda)$. $\sigma_{sum,cuts}$ is calculated analytically by integrating over the phase space allowed by the cuts the squared amplitude for the LQ process and its interference with NC DIS. The cuts applied, by reducing the NC DIS contribution, ensure that $\sigma_{sum,cuts}$ is positive for reasonable λ values.
- The event generator LEGO is then used to produce LQ events at (M_{LQ}, λ_0) , from which we get the acceptance correction factor A defined as the ratio of the number of events satisfying the NC DIS selection cuts as well as the M_e and y_e cuts, to the number of events generated within these cuts.

- To take into account next-to-leading order QCD corrections on the LQ production cross-section, we calculate the convolution K^* of the K-factor given in [28] for the NWA, with the LQ Breit-Wigner distribution corresponding to (M_{LQ}, λ_0) . The resulting function $K^*(M_{LQ})$ will be used henceforth to calculate the signal cross-sections. The NLO corrections lead to a sizeable enhancement of the cross-section as will be seen below.

- The final rejected coupling is then obtained by solving the equation $N_{lim} = \mathcal{L} \times A \times K^* \times \sigma_{sum,cuts}(\lambda)$.

The resulting rejection limits at 95% confidence level (CL) are shown in Fig. 13 up to $M_{LQ} = 400$ GeV for $|F| = 0$ or 2 scalars or vectors. Constraints for even larger masses where one is probing “strong” (i.e. $\lambda > 1$) coupling values in a contact interaction will be discussed in a separate paper. The case of $|F| = 0$ LQs, which can be produced via fusion between the e^+ and an incident valence quark, naturally offers the best sensitivity.

For LQs having $F = 0$, these limits represent an improvement by a factor $\simeq 3$ compared to H1 published results [11]. For a Yukawa coupling of the electromagnetic strength $\lambda^2/4\pi = \alpha_{EM}$ (i.e. $\lambda \simeq 0.3$), such scalar (vector) LQs are excluded at 95% CL up to 275 GeV (284 GeV) by this analysis. As can be seen in Fig. 13b the $S_{1/2,R}$ is the scalar for which HERA has the highest sensitivity since both charge states can be produced via a fusion e^+u or

e^+d . On the contrary, only an e^+u (e^+d) fusion is possible for the production of $S_{1/2,L}$ ($\tilde{S}_{1/2,L}$), for which the cross-sections are thus smaller. Note also that, due to the more favorable parton density, a higher cross-section (and thus a better rejection limit) is expected for $S_{1/2,L}$ than for $\tilde{S}_{1/2,L}$. However at very high masses, the $S_{1/2,L}$ interferes destructively with NC DIS, on the contrary to the $\tilde{S}_{1/2,L}$, so that the limits become similar.

For $|F|=2$ leptoquarks, the improvement compared to our previous published results is less substantial since e^-p data collected in 1994 had been also taken into account in [11]. These LQs will be best probed with e^-p data which are being collected since 1998.

For coupling values equal to the obtained limits, NLO QCD corrections enhance the production cross-section of a $F=0$ LQ by $\simeq 10\%$ for $M_{LQ} = 100$ GeV to $\simeq 30\%$ at 250 GeV. For higher masses this enhancement decreases because of the distortion of the LQ mass spectrum. For $|F|=2$ LQ, this enhancement remains below $\simeq 20\%$.

$S_{1,L}$ and $S_{0,L}$ leptoquarks being allowed to undergo CC DIS-like decays with a branching ratio $\beta_\nu = 0.5$, the combination of NC and CC DIS analysis is expected to better constrain these leptoquarks. The result of this combination is given for the $S_{0,L}$ by the curve $\beta_e = \beta_\nu = 0.5$ in Fig. 14a. It can be seen that combining the two contributing channels improves the sensitivity on $S_{0,L}$ up to that achieved on $S_{0,R}$, recalled on Fig. 14a by the curve $\beta_e = 1$.

The DELPHI [45] experiment at LEP recently performed a direct search for single leptoquarks using data accumulated at e^+e^- centre of mass energies $\sqrt{s_{e^+e^-}}$ up to 183 GeV. Constraints relevant for some LQ species have also been obtained indirectly by ALEPH [46], OPAL [47] and L3 [48] Collaborations from measurements of hadronic cross-sections and asymmetries at $\sqrt{s_{e^+e^-}} = 130$ to 183 GeV. For a Yukawa coupling of the electromagnetic strength, the direct search via single production results in a limit of 171 GeV which is not yet competitive with this H1 analysis. For similar coupling values, the indirect search at LEP is yet only competitive for the $S_{0,L}$, $S_{1,L}$, $V_{0,L}$, $\tilde{V}_{0,R}$ and $V_{1,L}$, for which limits up to 240 GeV and 470 GeV have been obtained in the scalar and vector case respectively. However the sensitivity of the indirect search drops quickly with the Yukawa coupling, and for $\lambda = 0.1$ bounds lie below 100 GeV for all LQ species [47].

In contrast to an ep collider, the limits derived at the TeVatron where LQs are mostly produced in pair via the strong interaction, with larger cross-sections expected for vector than for scalar leptoquarks, are essentially independent of the Yukawa coupling. Recent results have been published for scalar leptoquarks by $D\emptyset$ [49] and CDF [50] Collaborations. In the BRW model, a combination of these results [51] excludes scalar leptoquark masses up to 242 GeV. Comparisons of our results with limits obtained at the TeVatron collider in more general models will be presented in Sects. 6.5 and 6.6.

6.5 Mass dependent limits on the Yukawa coupling in generic models

Moving away from the BRW model, we now consider leptoquarks for which the branching ratios β_e and β_ν in NC and CC DIS-like decays are free parameters. As an example, the 95% CL exclusion contour for a scalar LQ with $|F|=2$ decaying with $\beta_\nu = 90\%$ in νq and $\beta_e = 10\%$ in eq is shown in Fig. 14a as the dash-dotted line. In this case, limits are shown only in the mass domain where the interference of LQ processes with DIS can be neglected. The gain obtained by the combination of both channels can be seen when comparing this contour with the greyed domain showing the sensitivity achieved using only NC DIS-like channel. For $\beta_\nu = 90\%$ and $\beta_e = 10\%$, scalar LQ masses below 200 GeV are excluded at 95% CL by our analysis, for Yukawa couplings of the electromagnetic strength. This extends far beyond the domain excluded by TeVatron experiments [49, 50] which for such small values of β_e only exclude scalar leptoquark masses below $\simeq 110$ GeV. At HERA the sensitivity will be considerably enhanced with an electron incident beam where these LQs can be produced via a fusion with a *valence* u quark. Hence a large discovery potential is opened for HERA, for high mass leptoquarks decaying in νq with a high branching ratio.

Similar results are given for a vector LQ coupling to e^+d in Fig. 14b. For the above values of (β_e, β_ν) and of the Yukawa coupling, the excluded mass domain extends in this case to 250 GeV.

6.6 Mass dependent limits on $\beta(LQ \rightarrow eq)$

We consider here leptoquarks which undergo NC DIS-like decays with a branching ratio β_e and do not make any assumption on the other possible decay modes of the LQ. For a fixed value of the Yukawa coupling λ upper limits on LQ production cross-section are translated in terms of mass dependent limits on the branching β_e . Exclusion limits at 95% CL are shown in Fig. 15a,b as greyed areas for scalar LQs produced via a e^+d or e^+u fusion respectively. On Fig. 15a, the central limit contour for $\lambda = 0.1$ has been obtained assuming an uncertainty on the d quark density distribution which varies with x as mentioned in Sect. 3. Curves above and below this contour define the error band obtained when the lack of knowledge on the proton structure is directly applied on the parton densities, instead of entering as a systematic uncertainty: the d quark density is enhanced/lowered by a factor varying linearly between 7% at low masses and up to 30% at 250 GeV. For LQs coupling to e^+u (Fig. 15b), a constant scaling factor of $\pm 7\%$ has been applied on the quite well-known u density, resulting in a much narrower error band.

Despite the small λ values considered, domains excluded by this analysis extend beyond the region covered by the $D\emptyset$ experiment [49] at the TeVatron also in the less favourable case of LQs coupling to e^+d . This is especially the case for small values of β_e . For example, for $\beta_e = 10\%$, this analysis rules out masses below $\simeq 240$ GeV

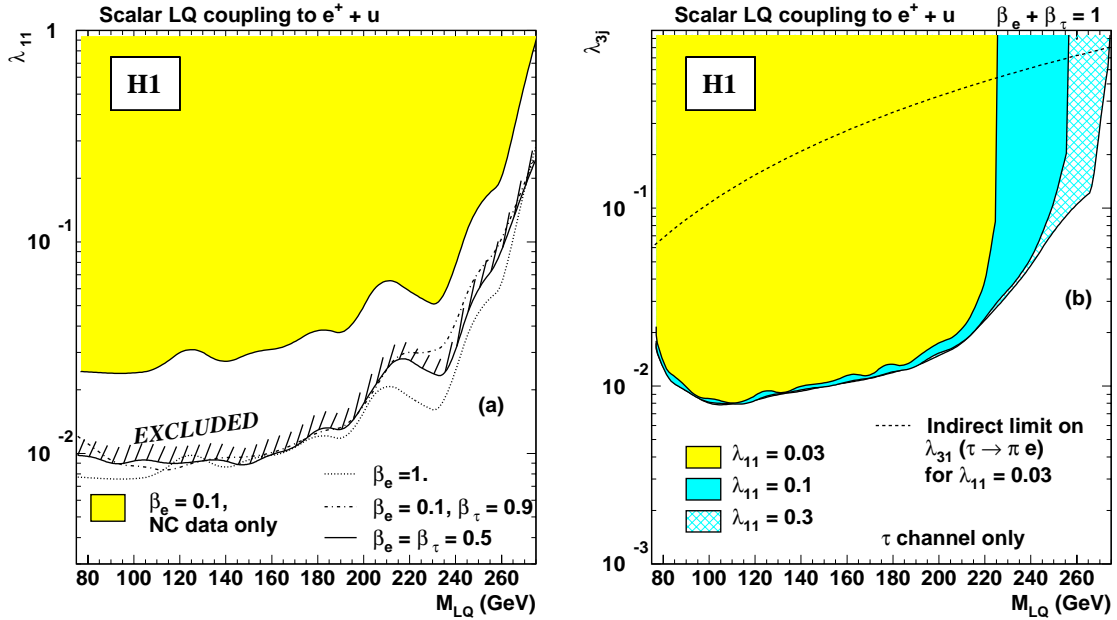


Fig. 16a,b. (a) Mass dependent exclusion limits at 95% CL on the Yukawa coupling λ_{11} , for scalar leptoquarks produced by e^+u fusion. Different hypotheses for the branching ratios into eq , τq are considered. Domains above the curves are excluded. (b) Exclusion domains in the plane λ_{3j} ($j = 1, 2$) against the leptoquark mass for several fixed values of λ_{11} (greyed areas). A mass dependent indirect limit on λ_{31} is also represented by the dashed line

($\simeq 200$ GeV) if $\lambda = 0.1$ ($\lambda = 0.05$) independently of other possible decay modes of the leptoquark, as can be seen in Fig. 15b. This limit extends up to 260 GeV for an electromagnetic strength of the Yukawa coupling λ as will be shown by the greyed domain in Fig. 16a. Hence, a yet unexplored region in the high mass - low β_e domain is probed by this analysis.

7 Constraints on couplings to mixed generations

In this section, we consider LFV LQs which couple to both the electron and a second or third generation lepton.

The case of low mass ($M < \sqrt{s_{ep}}$) LFV LQs is first addressed in Sect. 7.1. The analysis is there restricted to LQs possessing a coupling λ_{11} , allowing the LQ to be produced or exchanged between the incident lepton and a *valence* quark coming from the proton. Moreover we do not consider $e \leftrightarrow \mu$ transitions induced by a low mass LQ, such processes being strongly constrained by low energy experiments as will be seen in Sect. 7.2 where high mass ($M > \sqrt{s_{ep}}$) LFV LQs are considered. In this latter case, the study will be extended to any λ_{1i} , and both λ_{2j} and λ_{3j} .

7.1 Low mass ($M < \sqrt{s_{ep}}$) LFV leptoquarks

We now consider LFV LQs possessing a coupling λ_{11} to first generation lepton-quark pairs as well as a coupling λ_{3j} with leptons of the third generation.

Mass dependent exclusion limits on λ_{11} at 95% CL are shown in Fig. 16a when fixing the relative branching fractions β_e and β_τ into $e + jet$ and $\tau + jet$ final states. A generic scalar leptoquark coupling to $e^+ + u$ pairs (such as the $S_{1/2,L}$ in the BRW model) has been considered for three different sets of (β_e, β_τ) . Here both $e^+ + jet$ and $\tau^+ + jet$ channels are combined. This latter channel is background free but the former benefits from a higher selection efficiency, such that finally both provide a comparable sensitivity to the signal. Thus, as soon as $\beta_e + \beta_\tau$ approaches 1, the limits derived are very similar to those obtained for $\beta_e = 1$. Assuming $\beta_e = 10\%$ and $\beta_\tau = 90\%$, masses below 275 GeV are excluded at 95% CL for an electromagnetic strength of the λ_{11} coupling. Such limits are especially interesting since, for small β_e and high β_τ , the mass domain excluded by the TeVatron does not extend very far. The CDF experiment has performed a search for third generation LQs looking at $\tau\tau bb$ final states [52], and excluded scalar LQs with masses below 99 GeV if $\beta(LQ \rightarrow \tau b) = 1$. A complementary search has been carried out by $D0$ [53], where the analysis of $\nu\nu bb$ final states leads to a lower mass limit of 94 GeV for $\beta(LQ \rightarrow \nu b) = 1$. HERA thus appears to provide access to an unexplored domain for LQs decaying with a small branching ratio in eq and a high branching ratio in τq .

An alternative representation of our results is given in Fig. 16b in the plane λ_{3j} against the LQ mass, for different fixed values of λ_{11} . We consider here a scalar LQ formed via e^+u fusion (carrying the quantum numbers of the $S_{1/2,L}$ in the BRW model) such that only couplings λ_{3j} with $j = 1, 2$ are relevant and make the additional assumption that $\beta_e + \beta_\tau = 1$. The $\tau + jet$ final states analysis provides a sensitivity on λ_{31} so long as the LQ

$e \longleftrightarrow \mu$		$F = 0$					
BEST EXCLUSION UPPER LIMITS ON $\frac{\lambda_{1i} \lambda_{2j}}{M_{LQ}^2}$ (in 10^{-4} GeV^{-2})							
FOR LEPTON FLAVOUR VIOLATING LEPTOQUARKS							
$q_i q_j$	$S_{1/2,L}$	$S_{1/2,R}$	$\tilde{S}_{1/2,L}$	$V_{0,L}$	$V_{0,R}$	$\tilde{V}_{0,R}$	$V_{1,L}$
1 1	$\mu N \rightarrow e N$ 7.6×10^{-7} H1: 0.025	$\mu N \rightarrow e N$ 2.6×10^{-7} H1: 0.021	$\mu N \rightarrow e N$ 7.6×10^{-7} H1: 0.036	$\mu N \rightarrow e N$ 2.6×10^{-7} H1: 0.031	$\mu N \rightarrow e N$ 2.6×10^{-7} H1: 0.031	$\mu N \rightarrow e N$ 2.6×10^{-7} H1: 0.025	$\mu N \rightarrow e N$ 1.1×10^{-7} H1: 0.011
1 2	$D \rightarrow \mu e^+$ 0.062 H1: 0.026	$K \rightarrow \mu e^+$ 6×10^{-7} H1: 0.021	$K \rightarrow \mu e^+$ 6×10^{-7} H1: 0.036	$K \rightarrow \mu e^+$ 3.6×10^{-7} H1: 0.034	$K \rightarrow \mu e^+$ 3.6×10^{-7} H1: 0.034	$D \rightarrow \mu e^+$ 0.03 H1: 0.028	$K \rightarrow \mu e^+$ 3.6×10^{-7} H1: 0.013
1 3	*	$B \rightarrow \mu e$ 0.008 H1: 0.037	$B \rightarrow \mu e$ 0.008 H1: 0.037	V_{bu} 0.002 H1: 0.04	$B \rightarrow \mu e$ 0.004 H1: 0.04	*	V_{bu} 0.002 H1: 0.04
2 1	$D \rightarrow \mu e^+$ 0.062 H1: 0.089	$K \rightarrow \mu e^+$ 6×10^{-7} H1: 0.055	$K \rightarrow \mu e^+$ 6×10^{-7} H1: 0.070	$K \rightarrow \mu e^+$ 3.6×10^{-7} H1: 0.041	$K \rightarrow \mu e^+$ 3.6×10^{-7} H1: 0.041	$D \rightarrow \mu e^+$ 0.03 H1: 0.043	$K \rightarrow \mu e^+$ 3.6×10^{-7} H1: 0.019
2 2	$\mu \rightarrow e \gamma$ 2.8×10^{-5} H1: 0.11	$\mu \rightarrow e \gamma$ 2.8×10^{-5} H1: 0.062	ZEUS: 0.20 H1: 0.075	$\mu \rightarrow e \gamma$ 0.04 H1: 0.049	$\mu \rightarrow e \gamma$ 0.04 H1: 0.049	$\mu \rightarrow e \gamma$ 0.005 H1: 0.07	$\mu \rightarrow e \gamma$ 0.003 H1: 0.03
2 3	*	$B \rightarrow \bar{\mu} e K$ 0.006 H1: 0.084	$B \rightarrow \bar{\mu} e K$ 0.006 H1: 0.084	$B \rightarrow \bar{\mu} e K$ 0.003 H1: 0.078	$B \rightarrow \bar{\mu} e K$ 0.003 H1: 0.078	*	$B \rightarrow \bar{\mu} e K$ 0.003 H1: 0.078
3 1	*	$B \rightarrow \mu e$ 0.008 H1: 0.1	$B \rightarrow \mu e$ 0.008 H1: 0.1	V_{bu} 0.002 H1: 0.04	$B \rightarrow \mu e$ 0.004 H1: 0.04	*	V_{bu} 0.002 H1: 0.04
3 2	*	$B \rightarrow \bar{\mu} e K$ 0.006 H1: 0.11	$B \rightarrow \bar{\mu} e K$ 0.006 H1: 0.11	$B \rightarrow \bar{\mu} e K$ 0.003 H1: 0.05	$B \rightarrow \bar{\mu} e K$ 0.003 H1: 0.05	*	$B \rightarrow \bar{\mu} e K$ 0.003 H1: 0.05
3 3	*	ZEUS: 0.29 H1: 0.15	ZEUS: 0.29 H1: 0.15	$\mu \rightarrow e \gamma$ 5.6×10^{-4} H1: 0.108	$\mu \rightarrow e \gamma$ 5.6×10^{-4} H1: 0.108	*	$\mu \rightarrow e \gamma$ 5.6×10^{-4} H1: 0.108

Fig. 17. Rejection limits at 95% on $\lambda_{1i}\lambda_{2j}/M_{LQ}^2$ in units of 10^{-4} GeV^{-2} for $F = 0$ leptoquarks, compared to constraints from indirect processes. The first column indicates the generations of the quarks q_i and q_j coupling respectively to $LQ - e$ and $LQ - \mu$. In each box, the process which provides a most [22] stringent indirect constraint is listed (first line) together with its exclusion limit (second line) and compared to the actual H1 result (third line). Shaded boxes emphasize where HERA limit is comparable to (within a factor of 2) or better than the indirect constraints. The open boxes marked with a * are cases which would involve a top quark

is light enough to have a substantial production cross-section via λ_{11} , as can be seen on the 95% CL exclusion domains shown in Fig. 16b. For both couplings λ_{11} and λ_{3j} of the electromagnetic strength, such LQs lighter than 270 GeV are excluded at 95% CL. This limit still reaches 237 GeV for LQs formed by e^+d fusion (not shown). A similar lepton flavour violation analysis has been carried out by ZEUS Collaboration [13] using an integrated luminosity of $\simeq 3 \text{ pb}^{-1}$. For $\lambda_{11} = \lambda_{3j} = 0.03$, the analysis presented here extends their excluded mass range by $\simeq 65 \text{ GeV}$. Also shown in Fig. 16b is the best indirect limit [22] on λ_{31} in the case $\lambda_{11} = 0.03$. This indirect constraint comes from the upper limit on the branching ratio $\beta(\tau \rightarrow \pi^0 e)$ which could be affected by the process $\tau^+ \rightarrow \bar{u} + LQ$ followed by the $e^+ + u$ decay of the virtual leptoquark. Here the most recent upper limit [54] on $\beta(\tau \rightarrow \pi^0 e)$ has been used to update the bound derived in [22]. The H1 direct limit improves this indirect constraint by typically one order of magnitude. No low energy pro-

cess constrains the coupling products involving λ_{32} . In this case, H1 covers a yet unexplored domain.

It should be noted however that for most other LFV LQ species (except namely $\tilde{V}_{0,R}$, $S_{0,R}$ and $\tilde{V}_{1/2,L}$) the coupling products involving λ_{32} and λ_{33} can be constrained by low energy experiments, in particular by $\tau \rightarrow K^0 e$, $B \rightarrow \tau e X$, V_{ub} measurements or $K \rightarrow \pi \nu \bar{\nu}$ [22]. This latter process yields the most severe bound, relevant for $\lambda_{11} \times \lambda_{32}$, but which for $F = 0$ LQs only applies to those possessing the quantum numbers of the $V_{1,L}$ in the BRW model. It has been checked (not shown here) that for all other $F = 0$ LQs, the H1 direct limits on these coupling products extend beyond the domain covered by low energy phenomena. More detailed comparisons of HERA sensitivity with indirect bounds will be discussed in the next section.

$e \leftrightarrow \mu$ $F = 2$							
BEST EXCLUSION UPPER LIMITS ON $\frac{\lambda_{1i} \lambda_{2j}}{M_{LQ}^2}$ (in 10^{-4} GeV^{-2})							
FOR LEPTON FLAVOUR VIOLATING LEPTOQUARKS							
$q_i q_j$	$S_{0,L}$	$S_{0,R}$	$\tilde{S}_{0,R}$	$S_{1,L}$	$V_{1/2,L}$	$V_{1/2,R}$	$\tilde{V}_{1/2,L}$
1 1	$\mu N \rightarrow e N$ 7.6×10^{-7} H1: 0.051	$\mu N \rightarrow e N$ 7.6×10^{-7} H1: 0.051	$\mu N \rightarrow e N$ 7.6×10^{-7} H1: 0.061	$\mu N \rightarrow e N$ 2.3×10^{-7} H1: 0.026	$\mu N \rightarrow e N$ 2.6×10^{-7} H1: 0.018	$\mu N \rightarrow e N$ 1.5×10^{-7} H1: 0.010	$\mu N \rightarrow e N$ 2.6×10^{-7} H1: 0.013
1 2	$K \rightarrow \pi \nu \bar{\nu}$ 10^{-5} H1: 0.091	$D \rightarrow \mu \bar{e}$ 0.062 H1: 0.091	$K \rightarrow \mu \bar{e}$ 6×10^{-7} H1: 0.081	$K \rightarrow \mu \bar{e}$ 3.6×10^{-7} H1: 0.037	$K \rightarrow \mu \bar{e}$ 3.6×10^{-7} H1: 0.034	$K \rightarrow \mu \bar{e}$ 3.6×10^{-7} H1: 0.027	$D \rightarrow \mu \bar{e}$ 0.03 H1: 0.044
1 3	V_{ub} 0.004	*	$B \rightarrow \mu \bar{e}$ 0.008 H1: 0.086	V_{ub} 0.004 H1: 0.043	$B \rightarrow \mu \bar{e}$ 0.004 H1: 0.048	$B \rightarrow \mu \bar{e}$ 0.004 H1: 0.048	*
2 1	$K \rightarrow \pi \nu \bar{\nu}$ 10^{-5} H1: 0.055	$D \rightarrow \mu \bar{e}$ 0.062 H1: 0.055	$K \rightarrow \mu \bar{e}$ 6×10^{-7} H1: 0.066	$K \rightarrow \mu \bar{e}$ 3.6×10^{-7} H1: 0.029	$K \rightarrow \mu \bar{e}$ 3.6×10^{-7} H1: 0.018	$K \rightarrow \mu \bar{e}$ 3.6×10^{-7} H1: 0.011	$D \rightarrow \mu \bar{e}$ 0.03 H1: 0.013
2 2	$\mu \rightarrow e \gamma$ 1.1×10^{-4} H1: 0.13	$\mu \rightarrow e \gamma$ 1.1×10^{-4} H1: 0.13	$\mu \rightarrow e \gamma$ 4.5×10^{-5} H1: 0.095	$\mu \rightarrow e \gamma$ 2.2×10^{-5} H1: 0.045	$\mu \rightarrow e \gamma$ 0.08 ^Z H1: 0.037	$\mu \rightarrow e \gamma$ 0.003 H1: 0.030	$\mu \rightarrow e \gamma$ 0.003 H1: 0.052
2 3	$B \rightarrow l \nu X$ 0.04	*	$B \rightarrow \bar{\mu} e K$ 0.006 H1: 0.10	$B \rightarrow \bar{\mu} e K$ 0.003 H1: 0.052	$B \rightarrow \bar{\mu} e K$ 0.003 H1: 0.054	$B \rightarrow \bar{\mu} e K$ 0.003 H1: 0.054	*
3 1	V_{ub} 0.004	*	$B \rightarrow \mu \bar{e}$ 0.008 H1: 0.077	V_{ub} 0.004 H1: 0.038	$B \rightarrow \mu \bar{e}$ 0.004 H1: 0.018	$B \rightarrow \mu \bar{e}$ 0.004 H1: 0.018	*
3 2	$B \rightarrow l \nu X$ 0.04	*	$B \rightarrow \bar{\mu} e K$ 0.006 H1: 0.14	$B \rightarrow \bar{\mu} e K$ 0.003 H1: 0.068	$B \rightarrow \bar{\mu} e K$ 0.003 H1: 0.040	$B \rightarrow \bar{\mu} e K$ 0.003 H1: 0.040	*
3 3		*	$\mu \rightarrow e \gamma$ 4.5×10^{-5} H1: 0.17	$\mu \rightarrow e \gamma$ 2.2×10^{-5} H1: 0.085	$\mu \rightarrow e \gamma$ 0.006 H1: 0.068	$\mu \rightarrow e \gamma$ 0.006 H1: 0.068	*

Fig. 18. Rejection limits on $\lambda_{1i} \lambda_{2j} / M_{LQ}^2$ in units of 10^{-4} GeV^{-2} for $|F| = 2$ leptoquarks, compared to constraints from indirect processes. The first column indicates the generations of the quarks q_i and q_j coupling respectively to $LQ - e$ and $LQ - \mu$. In each box, the process which provides a most [22] stringent indirect constraint is listed (first line) together with its exclusion limit (second line) and compared to the actual H1 result (third line). Shadowed boxes emphasize where HERA limit is comparable to (within a factor of 2) or better than the indirect constraints. The superscripts Z indicate where earlier HERA [13] results already improved indirect bounds. The open boxes marked with a * are cases which would involve a top quark

7.2 High mass ($M > \sqrt{s_{ep}}$) LFV leptoquarks

In this section, we make use of the fact that no $\mu + jet$ or $\tau + jet$ candidate was found (with kinematic properties compatible with a $2 \rightarrow 2$ body process) to set constraints on very high mass LFV leptoquarks. For LQ masses well above the kinematic limit, the cross-section $\sigma(e^+ + p \rightarrow l_n^+ + jet + X)$ depends only on $(\lambda_{1i} \lambda_{nj} / M_{LQ}^2)^2$, with i and j indexing the generation of the quark coupling to $LQ - e$ and $LQ - l_n$ respectively, and where $l_n = \mu$ for $n = 2$ and $l_n = \tau$ for $n = 3$.

The 95% CL rejection limits are given for a $e \leftrightarrow \mu$ transition in Fig. 17 for $F = 0$ and Fig. 18 for $|F| = 2$ leptoquarks. Results are obtained for all possible quarks involved, q_i being the quark coupling to $LQ - e$ and q_j the one coupling to $LQ - \mu$. The limits are given in units of 10^{-4} GeV^{-2} . For processes involving a b quark in the initial state ($i = 3$ or $j = 3$), it has been checked that the correction to the cross-section due to the finite mass of the b remains below $\sim 5\%$ [55]. Early HERA results were

presented in a similar representation by the ZEUS Collaboration in [13]. The nomenclature defined in Table 2 has been kept to distinguish all possible LQ quantum numbers. Also given for each entry in the depicted tables are the constraints from the indirect process which currently provides the most stringent bound [22]. Figures 19 and 20 show similar limits for the $e \leftrightarrow \tau$ transition.

In Figs. 17-20, the bounds derived in [22] have been updated to take into account the latest results on suppressed or forbidden decays [54], and on the $\mu - e$ nuclear conversion [56]. Significant such updates concern in particular D and K decays into μe , $B \rightarrow \mu e$ [57] as well as $K \rightarrow \pi \nu \bar{\nu}$, $\tau \rightarrow \pi e$, $\tau \rightarrow e \gamma$ and $\mu \rightarrow e \gamma$ [58]. Previous HERA results [13], now superseded, are given in cases where there exists no known indirect constraint.

Provided that the quarks involved do not both belong to the first generation, it is seen that in some cases H1 limits supersede or come close to existing indirect bounds. For LQs coupling to muons, this concerns in particular the leptoquarks which can contribute to $\mu \rightarrow e \gamma$ and $D \rightarrow \mu e$

$e \longleftrightarrow \tau$		$F = 0$					
BEST EXCLUSION UPPER LIMITS ON $\frac{\lambda_{1i} \lambda_{3j}}{M_{LQ}^2}$ (in 10^{-4} GeV^{-2})							
FOR LEPTON FLAVOUR VIOLATING LEPTOQUARKS							
q_i, q_j	$S_{1/2,L}$	$S_{1/2,R}$	$\tilde{S}_{1/2,L}$	$V_{0,L}$	$V_{0,R}$	$\tilde{V}_{0,R}$	$V_{1,L}$
1 1	$\tau \rightarrow \pi e$ 0.0032 H1: 0.046	$\tau \rightarrow \pi e$ 0.0016 H1: 0.037	$\tau \rightarrow \pi e$ 0.0032 H1: 0.062	G_F 0.002 H1: 0.015	$\tau \rightarrow \pi e$ 0.0016 H1: 0.015	$\tau \rightarrow \pi e$ 0.0016 H1: 0.013	G_F 0.002 H1: 0.0060
1 2	ZEUS: 0.12 H1: 0.047	$\tau \rightarrow K e$ 0.05 H1: 0.038	$\tau \rightarrow K e$ 0.05 H1: 0.063	$\tau \rightarrow K e$ 0.03 H1: 0.017	$\tau \rightarrow K e$ 0.03 H1: 0.017	ZEUS: 0.10 H1: 0.014	$K \rightarrow \pi \nu \bar{\nu}$ 2.5×10^{-6} H1: 0.0065
1 3	*	$B \rightarrow \tau \bar{e} X$ 0.08 H1: 0.065	$B \rightarrow \tau \bar{e} X$ 0.08 H1: 0.065	$B \rightarrow l \nu X$ 0.02 H1: 0.020	$B \rightarrow \tau \bar{e} X$ 0.04 H1: 0.020	*	$B \rightarrow l \nu X$ 0.02 H1: 0.020
2 1	ZEUS: 0.34 H1: 0.15	$\tau \rightarrow K e$ 0.05 H1: 0.095	$\tau \rightarrow K e$ 0.05 H1: 0.12	$\tau \rightarrow K e$ 0.03 H1: 0.020	$\tau \rightarrow K e$ 0.03 H1: 0.020	ZEUS: 0.10 H1: 0.023	$K \rightarrow \pi \nu \bar{\nu}$ 2.5×10^{-6} H1: 0.010
2 2	$\tau \rightarrow e \gamma$ 0.03 H1: 0.18	$\tau \rightarrow e \gamma$ 0.02 H1: 0.10	ZEUS: 0.48 H1: 0.13	ZEUS: 0.25 H1: 0.024	ZEUS: 0.25 H1: 0.024	ZEUS: 0.31 H1: 0.034	ZEUS: 0.13 H1: 0.014
2 3	*	$B \rightarrow \tau \bar{e} X$ 0.08 H1: 0.14	$B \rightarrow \tau \bar{e} X$ 0.08 H1: 0.14	$B \rightarrow l \nu X$ 0.02 H1: 0.035	$B \rightarrow \tau \bar{e} X$ 0.04 H1: 0.035	*	$B \rightarrow l \nu X$ 0.02 H1: 0.035
3 1	*	$B \rightarrow \tau \bar{e} X$ 0.08 H1: 0.16	$B \rightarrow \tau \bar{e} X$ 0.08 H1: 0.16	V_{ub} 0.002 H1: 0.022	$B \rightarrow \tau \bar{e} X$ 0.04 H1: 0.022	*	V_{ub} 0.002 H1: 0.022
3 2	*	$B \rightarrow \tau \bar{e} X$ 0.08 H1: 0.19	$B \rightarrow \tau \bar{e} X$ 0.08 H1: 0.19	$B \rightarrow l \nu X$ 0.02 H1: 0.026	$B \rightarrow \tau \bar{e} X$ 0.04 H1: 0.026	*	$B \rightarrow l \nu X$ 0.02 H1: 0.026
3 3	*	ZEUS: 0.72 H1: 0.23	ZEUS: 0.72 H1: 0.23	$\tau \rightarrow e \gamma$ 0.51 ^Z H1: 0.045	$\tau \rightarrow e \gamma$ 0.51 ^Z H1: 0.045	*	ZEUS: 0.38 H1: 0.045

Fig. 19. Rejection limits on $\lambda_{1i} \lambda_{3j} / M_{LQ}^2$ in units of 10^{-4} GeV^{-2} for $F = 0$ leptoquarks, compared to constraints from indirect processes. The first column indicates the generations of the quarks q_i and q_j coupling respectively to $LQ - e$ and $LQ - \tau$. In each box, the process which provides a most [22] stringent indirect constraint is listed (first line) together with its exclusion limit (second line) and compared to the actual H1 result (third line). For the $\tilde{S}_{1/2,L}$, which does not couple to the neutrino, limits on $\lambda_{11} \times \lambda_{32}$ and on $\lambda_{12} \times \lambda_{31}$ derived in [22] from $K \rightarrow \pi \nu \bar{\nu}$ have been replaced by the bounds obtained from $\tau \rightarrow K e$. Shadowed boxes emphasize where HERA limit is comparable to (within a factor of 2) or better than the indirect constraints. The superscripts Z indicate where earlier HERA [13] results already improved indirect bounds. The open boxes marked with a * are cases which would involve a top quark

processes. For LQs coupling to taus, this concerns more cases and in particular the leptoquarks which can contribute to $\tau \rightarrow K e$, $\tau \rightarrow e \gamma$ and various forbidden B decays. The sensitivity improves over indirect constraints by up to an order of magnitude and some cases are covered uniquely by HERA experiments.

8 Conclusions

First generation leptoquarks (LQs) as well as leptoquarks possessing lepton flavor violating couplings have been searched at the HERA collider using 1994 to 1997 H1 data in a mass range extending from 75 GeV to beyond the ep kinematic limit of $\sqrt{s_{ep}} \simeq 300$ GeV.

The search for leptoquarks which only couple to first generation fermions involved an analysis of very high Q^2 neutral (NC) and charged current (CC) deep-inelastic scattering data. The comparison of these data with Standard Model expectations has shown deviations in the Q^2 spec-

trum at $Q^2 \gtrsim 10000 \text{ GeV}^2$ which are less significant than those previously observed in 1994 to 1996. No significant clustering of events in excess of SM expectations has been found in the mass spectra for NC or CC-like events in the 1997 dataset alone. Exclusion domains for LQ masses and couplings have been derived.

For first generation leptoquarks of the Buchmüller-Rückl-Wyler (BRW) effective model, masses up to 275 GeV (284 GeV) are excluded for scalars (vectors) with a Yukawa coupling of electromagnetic strength, $\lambda = \sqrt{4\pi\alpha_{EM}} = 0.3$. Constraints on the LQ couplings have been established for $\lambda \lesssim 1.0$ for all LQ types for masses up to 400 GeV. For $\lambda = 0.3$ but in generic models with arbitrarily small decay branching ratio β_e into NC-like final states, the exclusion domain extends to 260 GeV for β_e as small as 10%, far beyond the present reach of other existing colliders.

No event candidate has been found with either $\mu + jet$ or $\tau + jet$ final states compatible with the production of

$e \longleftrightarrow \tau$		$F = 2$					
BEST EXCLUSION UPPER LIMITS ON $\frac{\lambda_{1i} \lambda_{3j}}{M_{LQ}^2}$ (in 10^{-4} GeV^{-2})							
FOR LEPTON FLAVOUR VIOLATING LEPTOQUARKS							
$q_i q_j$	$S_{0,L}$	$S_{0,R}$	$\tilde{S}_{0,R}$	$S_{1,L}$	$V_{1/2,L}$	$V_{1/2,R}$	$\tilde{V}_{1/2,L}$
1 1	G_F 0.003 H1: 0.026	$\tau \rightarrow \pi e$ 0.0032 H1: 0.026	$\tau \rightarrow \pi e$ 0.0032 H1: 0.031	G_F 0.003 H1: 0.013	$\tau \rightarrow \pi e$ 0.0016 H1: 0.030	$\tau \rightarrow \pi e$ 8×10^{-4} H1: 0.018	$\tau \rightarrow \pi e$ 0.0016 H1: 0.023
1 2	$K \rightarrow \pi \nu \bar{\nu}$ 10^{-5} H1: 0.046	$\tau \rightarrow K e$ ZEUS: 0.20 H1: 0.046	$\tau \rightarrow K e$ 0.05 H1: 0.041	$K \rightarrow \pi \nu \bar{\nu}$ 10^{-5} H1: 0.019	$K \rightarrow \pi \nu \bar{\nu}$ 5×10^{-6} H1: 0.060	$\tau \rightarrow K e$ 0.03 H1: 0.048	$\tau \rightarrow K e$ ZEUS: 0.16 H1: 0.078
1 3	V_{bu} 0.004	*	$B \rightarrow \tau \bar{e} X$ 0.08 H1: 0.044	V_{bu} 0.004 H1: 0.022	$B \rightarrow \tau \bar{e} X$ 0.04 H1: 0.084	$B \rightarrow \tau \bar{e} X$ 0.04 H1: 0.084	*
2 1	$K \rightarrow \pi \nu \bar{\nu}$ 10^{-5} H1: 0.028	$\tau \rightarrow K e$ ZEUS: 0.22 H1: 0.028	$\tau \rightarrow K e$ 0.05 H1: 0.034	$K \rightarrow \pi \nu \bar{\nu}$ 10^{-5} H1: 0.014	$K \rightarrow \pi \nu \bar{\nu}$ 5×10^{-6} H1: 0.031	$\tau \rightarrow K e$ 0.03 H1: 0.018	$\tau \rightarrow K e$ ZEUS: 0.06 H1: 0.023
2 2	$\tau \rightarrow e \gamma$ 0.075 H1: 0.067	$\tau \rightarrow e \gamma$ 0.075 H1: 0.067	$\tau \rightarrow e \gamma$ 0.045 H1: 0.048	$\tau \rightarrow e \gamma$ 0.015 H1: 0.023	ZEUS: 0.25 H1: 0.064	ZEUS: 0.19 H1: 0.053	ZEUS: 0.31 H1: 0.091
2 3	$B \rightarrow l \nu X$ 0.04	*	$B \rightarrow \tau \bar{e} X$ 0.08 H1: 0.053	$B \rightarrow l \nu X$ 0.04 H1: 0.026	$B \rightarrow \tau \bar{e} X$ 0.04 H1: 0.095	$B \rightarrow \tau \bar{e} X$ 0.04 H1: 0.095	*
3 1	$B \rightarrow l \nu X$ 0.04	*	$B \rightarrow \tau \bar{e} X$ 0.08 H1: 0.039	$B \rightarrow l \nu X$ 0.04 H1: 0.019	$B \rightarrow \tau \bar{e} X$ 0.04 H1: 0.031	$B \rightarrow \tau \bar{e} X$ 0.04 H1: 0.032	*
3 2	$B \rightarrow l \nu X$ 0.04	*	$B \rightarrow \tau \bar{e} X$ 0.08 H1: 0.069	$B \rightarrow l \nu X$ 0.04 H1: 0.034	$B \rightarrow \tau \bar{e} X$ 0.04 H1: 0.071	$B \rightarrow \tau \bar{e} X$ 0.04 H1: 0.071	*
3 3		*	$\tau \rightarrow e \gamma$ 0.045 H1: 0.086	$\tau \rightarrow e \gamma$ 0.015 H1: 0.043	ZEUS: 0.38 H1: 0.120	ZEUS: 0.38 H1: 0.12	*

Fig. 20. Rejection limits on $\lambda_{1i} \lambda_{3j} / M_{LQ}^2$ in units of 10^{-4} GeV^{-2} for $|F| = 2$ leptoquarks, compared to constraints from indirect processes. The first column indicates the generations of the quarks q_i and q_j coupling respectively to $LQ - e$ and $LQ - \tau$. In each box, the process which provides a most [22] stringent indirect constraint is listed (first line) together with its exclusion limit (second line) and compared to the actual H1 result (third line). Shaded boxes emphasize where HERA limit is comparable to (within a factor of 2) or better than the indirect constraints. The open boxes marked with a * are cases which would involve a top quark

a LQ with couplings mixing the first and second or third generation in the leptonic sector. The constraints derived on the Yukawa couplings extend for some LQ types and coupling products beyond the reach of other colliders as well as of low energy experiments.

Acknowledgements. We are grateful to the HERA machine group whose outstanding efforts made this experiment possible. We appreciate the immense effort of the engineers and technicians who constructed and maintain the detector. We thank the funding agencies for their financial support of the experiment. We wish to thank the DESY directorate for the hospitality extended to the non-DESY members of the Collaboration. We thank W. Buchmüller, M. Spira, R. Rückl and F. Schrempp for help and useful discussions.

References

1. J.C. Pati and A. Salam, Phys. Rev. D **10** (1974) 275; P. Langacker, Phys. Rep. **72** (1981) 185; H. Georgi and S.L. Glashow, Phys. Rev. Lett. **32** (1974) 438.
2. A. Dobado, M.J. Herrero and C. Muñoz, Phys. Lett. B **191** (1987) 449; J.F. Gunion, E. Ma, Phys. Lett. B **195** (1987) 257; R.W. Robinett, Phys. Rev. D **37** (1988) 1321; J.A. Grifols and S. Peris, Phys. Lett. B **201** (1988) 287.
3. B. Schrempp and F. Schrempp, Phys. Lett. B **153** (1985) 101, and references therein; J. Wudka, Phys. Lett. B **167** (1986) 337.
4. S. Dimopoulos and L. Susskind, Nucl. Phys. B **155** (1979) 237; S. Dimopoulos, Nucl. Phys. B **168** (1980) 69; E. Farhi, L. Susskind, Phys. Rev. D **20** (1979) 3404; *idem* Phys. Rep. **74** (1981) 277.
5. H1 Collaboration, C. Adloff et al., Z. Phys. C **74** (1997) 191.
6. ZEUS Collaboration, J. Breitweg et al., Z. Phys. C **74** (1997) 207.

7. M. Drees, Phys. Lett. B **403** (1997) 353; U. Bassler and G. Bernardi, Z. Phys. C **76** (1997) 223.
8. T.K. Kuo and T. Lee, Mod. Phys. Lett. A **12** (1997) 2367; K.S. Babu et al., Phys. Lett. B **402** (1997) 367; J.L. Hewett and T.G. Rizzo, Phys. Lett. B **403** (1997) 353; Z. Kunszt and W.J. Stirling, Z. Phys. C **75** (1997) 453; T. Plehn et al., Z. Phys. C **74** (1997) 611; C. Friberg, E. Norrbin and T. Sjöstrand, Phys. Lett. B **403** (1997) 329; J.K. Elwood and A.E. Faraggi, Nucl. Phys. B **512** (1998) 42; M. Heyssler and W.J. Stirling, Phys. Lett. B **407** (1997) 259; J. Blümlein, Proceed. of the 5th Int. Workshop on Deep Inelastic Scattering and QCD (DIS 97), Chicago, USA (14-18 April 1997) 5pp.; E. Keith and E. Ma, Phys. Rev. Lett. **79** (1997) 4318; N.G. Deshpande and B. Dutta, Phys. Lett. B **424** (1998) 313; J.L. Hewett and T.G. Rizzo, SLAC preprint PUB-7549 (August 1997) 45pp.; T.G. Rizzo, Proceed. of the Workshop on Physics Beyond the Desert 1997, Tegernsee, Germany (8-14 June 1997) 32pp.; Z. Xiao, RAL preprint TR-97-043 (September 1997) 26pp.; R. Rückl and H. Spiesberger, Proceed. of the Workshop on Physics Beyond the Desert, Tegernsee, Germany (8-14 Jun 1997) 18pp.; M. Sekiguchi, H. Wada and S. Ishida, Nihon University preprint NUP-A-97-23 (December 1997) 7 pp.
9. W. Buchmüller, R. Rückl and D. Wyler, Phys. Lett. B **191** (1987) 442. *Erratum* Phys. Lett. B **448** (1999) 320.
10. H1 Collaboration, C. Adloff et al., "Measurement of Neutral and Charged Current cross-sections in Positron-Proton Collisions at Large Momentum Transfer", To be submitted for publication.
11. H1 Collaboration, I. Abt et al., Nucl. Phys. B **396** (1993) 3; *idem*, T. Ahmed et al., Z. Phys. C **64** (1994) 545; *idem*, T. Ahmed et al., Phys. Lett. B **369** (1996) 173.
12. ZEUS Collaboration, M. Derrick et al., Phys. Lett. B **306** (1993) 173.
13. ZEUS Collaboration, M. Derrick et al., Z. Phys. C **73** (1997) 613.
14. H1 Collaboration, I. Abt et al., Nucl. Instr. and Meth. A **386** (1997) 310.; *idem* Nucl. Instr. and Meth. A **386** (1997) 348.; H1 Spacal Group, R. Appuhn et al., Nucl. Instr. and Meth. A **386** (1997) 397.
15. H1 Calorimeter Group, B. Andrieu et al., Nucl. Instr. and Meth. A **336** (1993) 460.
16. H1 Calorimeter Group, B. Andrieu et al., Nucl. Instr. and Meth. A **344** (1994) 492.
17. H1 Calorimeter Group, B. Andrieu et al., Nucl. Instr. and Meth. A **350** (1994) 57; *idem*, Nucl. Instr. and Meth. A **336** (1993) 499.
18. Ph. Bruel, Ph.D Thesis, Université de Paris-Sud, "Recherche d'interactions au-delà du Modèle Standard" (in French) (1998).
19. H1 SPACAL Group, R.D. Appuhn et al., Nucl. Instr. and Meth. A **386** (1997) 397.
20. H1 BEMC Group, J. Ban et al., Nucl. Instr. and Meth. A **372** (1996) 399.
21. T. Matsushita, E. Perez and R. Rückl, Contribution to the 3rd UK Phenomenology Workshop on HERA Physics, St. John's College, Durham, UK, September 1998, hep-ph/9812481, WUE-ITP-98-056, DAPNIA/SPP 98-23, 15pp.
22. S. Davidson, D. Bailey and B. Campbell, Z. Phys. C **61** (1994) 613.
23. M. Leurer, Phys. Rev. D **49** (1994) 333; *idem*. D **50** (1994) 536.
24. B. Schrempp, Proc. of the Workshop Physics at HERA, DESY, Hamburg (1991), vol. 2 p. 1034, and references therein.
25. LEGO 0.02 and SUSSEX 1.5; K. Rosenbauer, dissertation RWTH Aachen (in German), PITHA 95/16, July 1995.
26. JETSET 7.3 and 7.4; T. Sjöstrand, Lund University preprint LU-TP-95-20 (August 1995) 321pp; *idem*, CERN preprint TH-7112-93 (February 1994) 305pp.
27. V.N. Gribov et L.N. Lipatov, Sov. Journ. Nucl. Phys. **15** (1972) 78; G. Altarelli et G. Parisi, Nucl. Phys. B **126** (1977) 298; Y.L. Dokshitzer, JETP **46** (1977) 641.
28. T. Plehn et al., Z. Phys. C **74** (1997) 611.
29. A.D. Martin, R.G. Roberts, W.J. Stirling and R.S. Thorne, Euro. Phys. J. C **4** (1998) 463.
30. NA51 Collaboration, A. Baldit et al., Phys. Lett. B **332** (1994) 244.
31. E866 Collaboration, E.A. Hawker et al., Phys. Rev. Lett. **80** (1998) 3715.
32. H1 Collaboration, S. Aid et al., Nucl. Phys. B **470** (1996) 3.
33. ZEUS Collaboration, M. Derrick et al., Zeit. Phys. C **72** (1996) 399.
34. DJANGO 6.2; G.A. Schuler and H. Spiesberger, Proc. of the Workshop Physics at HERA, W. Buchmüller and G. Ingelman (Editors), (October 1991, DESY-Hamburg) Vol. 3 p. 1419.
35. HERACLES 4.4; A. Kwiatkowski, H. Spiesberger and H.-J. Möhring, Comput. Phys. Commun. **69** (1992) 155.
36. ARIADNE 4.08; L. Lönnblad, Comput. Phys. Commun. **71** (1992) 15.
37. G. Gustafson and U. Pettersson, Nucl. Phys. B **306** (1988) 746; *idem*, *addendum* Lund University preprint LU-TP-87-19, (October 1987) 4pp.; B. Andersson et al., Z. Phys. C **43** (1989) 625.
38. PYTHIA 5.6; T. Sjöstrand, Comp. Phys. Comm. **39** (1986) 347; T. Sjöstrand and M. Bengtsson, Comp. Phys. Comm. **43** (1987) 367.
39. M. Glück, E. Reya and A. Vogt, Phys. Rev. D **45** (1992) 3986; *idem*, Phys. Rev. D **46** (1992) 1973.
40. H1 generator based on EPVEC 1.0; U. Baur, J.A.M. Vermaseren and D. Zeppenfeld, Nucl. Phys. B **375** (1992) 3.
41. S. Baranov et al., Proc. of the Workshop Physics at HERA, W. Buchmüller and G. Ingelman (Editors), (October 1991, DESY-Hamburg) Vol. 3, p. 1478; J.A.M. Vermaseren, Nucl. Phys. B **229** (1983) 347.
42. S. Bentvelsen, J. Engelen and P. Kooijman, Proc. of the Workshop Physics at HERA, W. Buchmüller and G. Ingelman (Editors), (October 1991, DESY-Hamburg) Vol. 1 p. 25; K.C. Hoeger, *idem*. p. 43; and references therein.
43. A. Blondel, F. Jacquet, Proceedings of the Study of an ep Facility for Europe, ed. U. Amaldi, DESY report 79-48 (1979) 391.
44. H1 Collaboration, C. Adloff et al., Euro. Phys. J. C **5** (1998) 575.
45. DELPHI Collaboration, P. Abreu et al., Phys. Lett. B **446** (1999) 62.
46. ALEPH Collaboration, R. Barate et al., "Study of Fermion Pair Production in e^+e^- Collisions at 130 – 183 GeV", CERN-EP/99-042, Apr. 1999

47. OPAL Collaboration, G. Abbiendi et al., Euro. Phys. J. C **6** (1999) 1.
48. L3 Collaboration, M. Acciarri et al., Phys. Lett. B **433** (1998) 163.
49. DØ Collaboration, B. Abbott et al., Phys. Rev. Lett. **79** (1997) 4321; DØ Collaboration, B. Abbott et al., Phys. Rev. Lett. **80** (1998) 2051.
50. CDF Collaboration, F. Abe et al., Phys. Rev. Lett. **79** (1997) 4327.
51. LQ Limit Combination Working Group, for the CDF and DØ Collaborations, "Combined Limits on First Generation Leptoquarks from the CDF and D0 Experiments", hep-ex/9810015 (Oct. 98), 9pp.
52. CDF Collaboration, F. Abe et al., Phys. Rev. Lett. **78** (1997) 2906.
53. DØ Collaboration, B. Abbott et al., Phys. Rev. Lett. **81** (1998) 38.
54. Review of Particle Physics, European Phys. Journal C, Vol **3**, Nb 1-4 (1998).
55. M. Spira, Private Communication; see also A. Djouadi et al., Z. Phys. C **46** (1990) 679.
56. SINDRUM II Collaboration, S. Eggli et al., "Search for $\mu^- \rightarrow e^-$ Conversion on Titanium", submitted to Phys. Rev. C (1999).
57. CDF Collaboration, F. Abe et al., Phys. Rev. Lett. **81** (1998) 5742.
58. MEGA Collaboration, M.L. Brooks et al., LA-UR-99-2268, hep-ex/9905013.